PVRL2 Suppresses Antitumor Immunity through PVRIG- and TIGIT-independent Pathways

Jiuling Yang[1], Li Wang[1], James R. Byrnes[2], Lisa L. Kirkemo[2], Hannah Driks[1], Cassandra D. Belair[1], Oscar A. Aguilar[3], Lewis L. Lanier[3], James A. Wells[2], Lawrence Fong[4], and Robert Blelloch[1]

ABSTRACT

Poliovirus receptor-related 2 (PVRL2, also known as nectin-2 or CD112) is believed to act as an immune checkpoint protein in cancer; however, most insight into its role is inferred from studies on its known receptor, poliovirus receptor (PVR)-related immunoglobulin domain protein (PVRIG, also known as CD112R). Here, we study PVRL2 itself. PVRL2 levels were found to be high in tumor cells and tumor-derived exosomes. Deletion of PVRL2 in multiple syngeneic mouse models of cancer showed a dramatic reduction in tumor growth that was immune dependent. This effect was even greater than that seen with deletion of PD-L1. PVRL2 was shown to function by suppressing $CD8^+$ T and natural killer cells in the tumor microenvironment. The loss of PVRL2 suppressed tumor growth even in the absence of PVRIG. In contrast, PVRIG loss showed no additive effect in the absence of PVRL2. T-cell immunoreceptor with Ig and ITIM domains (TIGIT) blockade combined with PVRL2 deletion resulted in a near complete block in tumor growth. This effect was not recapitulated by the combined deletion of PVRL2 with its paralog, PVR, which is the ligand for TIGIT. These data uncover PVRL2 as a distinct inhibitor of the antitumor immune response with functions beyond that of its known receptor PVRIG. Moreover, the data provide a strong rationale for combinatorial targeting of PVRL2 and TIGIT for cancer immunotherapy.

Introduction

Over the past decade, immune checkpoint inhibitors (ICI), including antibodies blocking immune checkpoints PD-1, PD-L1, and CTLA-4, have made substantial progress in advancing cancer immunotherapy. These ICIs enhance the ability of the host immune system to combat cancer and have achieved remarkable success across numerous cancer types. Nevertheless, only 10%–30% of patients with cancer exhibit favorable responses to these therapies (1–4). Moreover, a majority of patients who initially respond eventually develop resistance during the course of treatment (1, 4). The underlying mechanisms responsible for the initial or acquired resistance to ICIs in a large percentage of patients remain mostly unknown. Therefore, it is of utmost importance to gain a better understanding of these mechanisms and identify additional immunotherapeutic strategies to overcome resistance to further improve cancer care.

Exosomes have emerged as a potential mechanism of resistance to ICIs (5–7). Exosomes are small extracellular vesicles ranging from 50 to 150 nm in diameter that originate from the endosome system of almost all mammalian cells, including tumors cells (8). Recent studies from our group and several others have demonstrated that tumor-derived exosomes can present PD-L1, thereby suppressing T-cell activation and promoting tumor growth across multiple cancer types (5, 6, 9, 10). However, PD-L1 is unlikely to fully explain the immunosuppressive properties of exosomes as anti-PD-L1/PD-1 blockade fails to fully recapitulate the loss of exosomes on the antitumor immune response and tumor growth (5, 6). Therefore, there is need to better understand the mechanisms underlying exosome-driven immune suppression.

In recent years, there has been a rapid lengthening of the list of potential immune checkpoint proteins, including members of the Nectin and Nectin-like family. In particular, the ligands poliovirus receptor-related 2 (PVRL2, also known as Nectin-2 or CD112) and poliovirus receptor (PVR, also known as Necl-5 or CD155) have been proposed to play immunoregulatory roles in tumor progression (11, 12). PVRL2 and PVR are expressed on tumor cells, antigen-presenting cells (APC), and endothelial cells (13). They interact with a costimulatory receptor DNAX accessory molecule 1 (DNAM-1, also known as CD226), which is expressed on T cells and natural killer (NK) cells, stimulating their activation (14–16). However, they also bind immunoinhibitory receptors, including T-cell immunoreceptor with Ig and ITIM domains protein (TIGIT), PVR-related immunoglobulin domain protein (PVRIG, also called CD112R), and CD96 (also known as TACTILE) (17–22). PVR serves as the primary ligand for TIGIT, while PVRL2 is thought to be the primary ligand for PVRIG (17–19). PVRL2 may also bind to TIGIT, but with low affinity (17, 18). PVR is also a ligand for CD96, although its role in regulating immune cells remains unclear due to conflicting results (20–23). Similar to other checkpoint receptors, such as PD-1, both TIGIT and PVRIG contain an immunoreceptor tyrosine-based inhibitory motif (ITIM) within their cytoplasmic tails (14, 17, 18), albeit truncated in mouse PVRIG (24). The binding affinities of PVR to TIGIT and PVRL2 to PVRIG are much higher than their affinities to DNAM-1 (17, 19, 25, 26). Thus, TIGIT and PVRIG may also function in part by outcompeting DNAM-1 for ligand binding (26, 27); however, mechanistic studies on these pathways are rather limited.

In recent years, the PVR–TIGIT and PVRL2–PVRIG pathways have been pursued as potential novel therapeutic targets for cancer. Blocking antibodies against TIGIT, PVRIG, and PVR have been

[1]Department of Urology, University of California San Francisco, San Francisco, California. [2]Department of Pharmaceutical Chemistry, University of California San Francisco, San Francisco, California. [3]Department of Microbiology and Immunology, University of California, San Francisco, and Parker Institute for Cancer Immunotherapy, San Francisco, California. [4]Division of Hematology/Oncology, Department of Medicine, University of California, San Francisco, San Francisco, California.

Corresponding Author: Robert Blelloch, University of California, San Francisco, 35 Medical Center Way, San Francisco, CA 94143. E-mail: robert.blelloch@ucsf.edu

Cancer Immunol Res 2024;12:575–91

doi: 10.1158/2326-6066.CIR-23-0722

developed and are currently in various stages of clinical trials. TIGIT was the first target to be evaluated for therapeutic development and many anti-TIGIT are currently undergoing phase I–III clinical trials, showing promising outcomes particularly when combined with anti-PD-1 or anti-PD-L1 therapies (28). More recently, an anti-PVRIG, COM701, has entered phase I clinical trials as monotherapy and in combination with an anti-PD-1 (nivolumab; NCT03667716), and with nivolumab and an anti-TIGIT (BMS-986207; NCT04570839) for solid tumors (29, 30). Another anti-PVRIG, NM1F, also entered phase I clinical trials in 2023 for advanced solid tumors (NCT05746897). Furthermore, an anti-PVR has been developed and entered in phase I clinical trials in 2022 (NCT05378425). No such efforts have been taken for PVRL2, likely at least in part because its functions are thought to be through PVRIG and thus targeting it could be considered redundant with current anti-PVRIG development strategies.

To date, very few studies have directly evaluated the role of PVRL2 in antitumor immunity and assessed its potential as a therapeutic target. Using mass spectrometry–based proteomics, we not only identified PVRL2 on tumor cells, but also tumor-derived exosomes. We performed follow-up genetic studies to show a partial role for PVRL2 on exosomes in promoting tumor growth, and an even larger role in this for PVRL2 on cells. Loss of PVRL2 showed a dramatic reduction in tumor growth by impacting both the adaptive and innate immune responses, while PVR mostly impacted the innate immune response. These effects were largely independent of PVRIG. Combinatorial inhibition of TIGIT, but not PVR, and loss of PVRL2 showed the largest effects. These data uncover PVRIG-independent roles for PVRL2 in the antitumor immune suppression and provide a strong rationale for targeting PVRL2 as a novel strategy in cancer care.

Materials and Methods

Cell lines

Human tumor cell lines

PC3 and SK-MEL-28 cell lines were purchased from ATCC, where they had been authenticated. PC3 is a prostatic adenocarcinoma cell line derived from a male patient (31). SK-MEL-28 is a malignant melanoma cell line isolated from a male patient (32). PC3 cells were cultured in F-12K Medium (Kaighn's Modification of Ham's F-12 Medium; GIBCO, ref. 21127-022), supplemented with 10% FBS (Corning, ref. 35-010-CV) and Penicillin/Streptomycin (Sigma, catalog no. P4333). SK-MEL-28 cells were cultured in ATCC-formulated Eagle's Minimum Essential Medium (ATCC, catalog no. 30-2003) with 10% FBS (Corning, ref. 35-010-CV) and Penicillin/Streptomycin (Sigma, catalog no. P4333). All cells were cultured at 37°C in a humidified atmosphere containing 5% CO_2.

Mouse tumor cell lines

TRAMP-C2, CT26, and B16F10 cells were obtained from ATCC, where they had been authenticated. MC38 cells were kindly provided by Dr. Jeffrey Schlom at the NCI at NIH, and were originally purchased from and authenticated by Kerafast. TRAMP-C2 cells are transgenic prostate adenocarcinoma cells derived from a C57BL/6 male mouse (33). CT26 cells are undifferentiated murine colon carcinoma cells derived from a female BALB/c mouse induced with N-nitroso-N-methylurethane-(34). B16F10 cells are a melanoma cell subline from B16 parental line derived from a male C57BL/6 mouse that has high lung metastatic ability (35). MC38 are murine colon adenocarcinoma cells derived from a female C57BL/6 (36).

TRAMP-C2 cells were cultured in DMEM (UCSF cell culture facility), with 5% Nu-Serum IV (Corning, catalog no. 80089-542), 5% FBS (Corning, ref. 35-010-CV), 0.005 mg/mL Bovine Insulin (Sigma, catalog no. I0516), 10 nmol/L DHEA (Sigma, catalog no. D-063), and Penicillin/Streptomycin (Sigma, catalog no. P4333). B16F10 cells were cultured in ATCC-formulated DMEM (ATCC, catalog no. 30-2002) with 10% FBS (Corning, ref. 35-010-CV) and Penicillin/Streptomycin (Sigma, catalog no. P4333). CT26 cells were cultured in RPMI1640 Medium (GIBCO, ref. A10491-01) with 10% FBS (Corning, ref. 35-010-CV) and Penicillin/Streptomycin (Sigma, catalog no. P4333). MC38 cells were cultured in DME H-21 (DMEM) High Glucose (UCSF cell culture facility) containing 10% FBS (Corning, ref. 35-010-CV), Penicillin/Streptomycin (Sigma, catalog no. P4333), 1 mmol/L sodium pyruvate (GIBCO, ref. 11360-070), 1% NEAA (GIBCO, ref. 11140-050), 0.05 mg/mL Gentamicin (GIBCO, ref. 15750-060). All cells were cultured at 37°C in a humidified atmosphere containing 5% CO_2.

All the cell lines used were obtained within the past decade. Early passage cells were cryogenically preserved in liquid nitrogen. The freshly thawed cells were cultured for approximately 1 week (2–3 passages) prior to use. The total number of passages for each cell line was limited to 20. All cell lines were confirmed to be *Mycoplasma* negative using the Mycoplasma PCR Detection Kit (Bulldog Bio, catalog no. 2523148) every 6 months.

Animals

Wild-type (WT) C57BL/6 mice (Stock no. 000664) and Balb/cJ mice (Stock no. 000651) were purchased from The Jackson Laboratory. Immunodeficient NOD CRISPR *Prdkc Il2r Gamma* (NCG) mice were purchased from Charles River (Stock no. 572). The *Pvrig* knockout (KO) mice were derived from sperm obtained through the NIH Knockout Mouse Project (KOMP) program from the Mutant Mouse Regional Resource Centers at UCDavis (Stock no. 043995-UCD). *In vitro* fertilization was performed at the University of California San Francisco (UCSF) Cryopreservation Core. The resulting mice were bred and genotyped by PCR (primer sequences are listed below). *Rag1* KO mice were kindly shared by Dr. Alexander Marson at UCSF and were originally purchased from The Jackson Laboratory (Stock no. 002216). Age-matched male mice ranging 8–11 weeks old were used for all experiments. Mice were randomly assigned to experimental or control groups. Mice were bred and housed under specific pathogen-free condition. All experiments were conducted under protocols preapproved by the Institutional Animal Care and Use Committee at UCSF (protocol no. AN188927) and guidelines set by the NIH. Animals were housed in an Association for Assessment and Accreditation of Laboratory Animal Care International accredited facility under OLAW assurance number D16-00253 (A3400-01).

Pvrig KO genotyping common forward primer: GTTCCATTCC-CTGCCCCTTAGC

Pvrig KO genotyping common reverse primer: CGTACTCTTCG-GCTCACACTTGTGT

Pvrig KO genotyping WT reverse primer: GCAATGTTGAGA-ATAGAACCAGGGTC

Primary tumor tissue

Deidentified human prostate tissues were obtained from the UCSF BIOS tissue bank. Human prostate slices were prepared and cultured as published previously (37). Briefly, 8 mm diameter cores of putative benign and cancerous regions were taken from the peripheral zones according to gross analysis. The cores were aseptically cut to approximately 300 mm thickness in the Krumdieck Tissue Slicer (Alabama Research and Development). Five tissue slices were transferred to the titanium mesh inserts in 6-well plates containing 2.5 mL of complete

PFMR-4A medium. Fully supplemented PFMR-4A media was kindly provided by Dr. Peehl at the UCSF Department of Radiology. The plates were incubated at 37°C in a humidified atmosphere containing 5% CO_2 on a 30° angled rotating platform. After 48 hours, media was removed and kept on ice for exosome preparation.

Exosome isolation and purification

To isolate exosomes from tumor cells, the cells were plated at a density of 3×10^6 cells per 15 cm plate for MC38, TRAMP-C2, CT26, and B16F10 cells or 5×10^6 cells per plate for PC3 and SK-MEL-28 cell lines and cultured in their complete media for 48 hours. To isolate exosomes from TRAMP-C2 cells for mass spectrometry, the cells were cultured in the complete media ± 10 ng/mL IFNγ (Abcam, catalog no. Ab9922) for 48 hours prior to exosome collection. Culturing of primary tumor tissue slices was performed as described above (see *Primary tumor tissue*). After culturing, exosomes were isolated from the media through differential ultracentrifugation by following our previously published protocol (5). In brief, pooled media from the cell or primary tissue culturing plates were spun at 300 × *g* for 10 minutes at room temperature to pellet cells. The supernatant was subsequently spun at 4°C at 2,000 × *g* for 20 minutes to pellet cell debris, 12,000 × *g* for 40 minutes to pellet microvesicles, and 100,000 × *g* for 70 minutes to pellet exosomes. The 100,000 × *g* pellet was resuspended in PBS and spun again at 100,000 × *g* for 70 minutes to wash the exosomes.

To purify exosomes from tumor cell lines or primary tissues for mass spectrometry, isolated exosomes were subjected to a sucrose density gradient. Exosomes were resuspended in 60% sucrose and loaded onto a gradient of 0%, 20%, 40% sucrose at increasing density. The gradient was spun at 4°C at 47,000 rpm for 16 hours. Sucrose fractions containing exosomes (20%–40%) were identified via a refractometer, diluted with 1 mL PBS, and spun at 4°C at 100,000 × *g* (50,000 rpm) for 3 hours to pellet purified exosomes.

Mass spectrometry

Isolated cell and exosome pellets from PC3 and SK-MEL-28 cells, and exosomes from primary tumors were processed and analyzed as described previously (38). Briefly, pellets were resuspended in chaotropic lysis buffer [50 mmol/L Tris pH 8.5, 6 mol/L guanidinium hydrocholoride, 5 mmol/L Tris (2-carboxy-ethyl)-phosphin-HCl, and 10 mmol/L chloroacetamide] and simultaneously lysed, reduced, and alkylated by heating at 97°C for 10 minutes with intermittent vortexing. Cell pellets were further disrupted using sonication. Samples were allowed to cool and insoluble debris removed by centrifugation (21,000 × *g*, 10 minutes). The resulting supernatant was diluted to 2 mol/L guanidinium hydrocholoride with 50 mmol/L Tris, pH 8.5 and protein concentration assessed by absorbance at 280 nm. Sequencing-grade trypsin (Promega) was added at a 1:100 ratio relative to total protein in the lysate and digestion allowed to proceed overnight at room temperature. After digestion, samples were desalted using SOLA HRP SPE columns (Thermo Fisher Scientific) following standard protocols. Eluted peptides were dried and resuspended in 0.1% formic acid with 2% acetonitrile. LC/MS-MS analysis was then performed on 1 μg of resuspended peptides using a Q Exactive Plus mass spectrometer as described previously (38, 39). Exosome samples from TRAMP-C2 cells were processed using the commercial Preomics iST kit and analyzed using a Bruker timsTOF Pro mass spectrometer as described previously (40). All proteomics data were evaluated using MaxQuant software. For data generated using the Q Exactive Plus mass spectrometer, data were analyzed, and label-free quantitation (LFQ) performed with MaxQuant version 1.5.1.2. Data were searched against the human proteome (SwissProt) with cysteine carbamidomethyl set as a fixed modification. N-terminal acetylation and methionine oxidation were set as variable modifications. Search results were filtered to a false discovery of 1% at both the peptide and protein levels. Data were visualized, processed, and compared using Perseus. Proteins with only one unique peptide were removed from analysis. LFQ intensities were $\log_2(x)$ transformed and missing values imputed using standard Perseus settings (width of 0.3, downshift of 1.8). Statistical differences between cell and exosome protein content for PC3 and SK-MEL-28 lines were determined using Student *t* test. For analysis of the TRAMP-C2 samples, MaxQuant version 1.6.6.0 was used to search data against the mouse proteome (SwissProt) and similarly triaged using Perseus. For functional gene enrichment analysis, all proteins detected in at least one PC3 or SK-MEL-28 exosome samples were analyzed by ShinyGO 0.77 (http://bioinformatics.sdstate.edu/go/) to identify immune regulation–related molecules. String network of the functional and physical protein–protein interactions of the identified exosomal immune regulators was generated from Sting-db, Version 11.5 (https://string-db.org/) with a confidence score 0.4 and above (41).

CRISPR/Cas9-mediated gene KO

The single-guide RNA (sgRNA) oligonucleotides (IDT DNA) targeting mouse *Pvrl2* or *Pvr* were cloned into pSpCas9(BB)-2A-GFP plasmid (PX458, ADDGENE). A total of 6 μg of each vector was transfected into tumor cells plated on a 6-well plate using FuGENE6 transfection reagent (Promega, catalog no. E2691) and OPTI-MEM (GIBCO, ref. 31985-062). A total of 48 hours after transfection, *Pvrl2* and *Pvr* KO clones were flow-sorted by GFP^+ single-cell cloning. After expansion, KO clones were identified by flow cytometry analysis for cell surface expression of PVRL2 or PVR (see *Immune profiling*). MC38 *Pvrl2*; *Pvr* double KO cells were generated by transfecting the *Pvr* sgRNA containing PX458 plasmid into MC38 *Pvrl2* KO cells using the same strategy. MC38 *Pdl1* KO cells were generated through CRISPR Cas9-gRNA RNP-directed deletion by using a Lonza 4D-Nucleofector and a SF Cell Line 4D-Nucleofector X Kit S (Lonza, catalog no. V4XC-2032). In brief, 65 pmol of sgRNA targeting mouse *Pdl1* (IDT DNA) and 30 pmol of S.p. Cas9 Nuclease (IDT, catalog no. 1081058) were mixed and incubated at 37°C for 10 minutes to form the Cas9–sgRNA RNP complex. MC38 cells were suspended in 20 μL SF buffer with supplement and then the RNP mixture was added to the cell suspension for nucleofection. Following nucleofection, cells were allowed to recover for 3 days, and then the $PD\text{-}L1^-$ population was purified by three rounds of flow-sorting. The sgRNA sequences were:

Mouse *Pvrl2* guide: GTCGGTGACAATCTGGACGG
Mouse *Pvr* guide: GAAATTCTTGGCTGCCCAAC
Mouse *Pdl1* guide: GTTTACTATCACGGCTCCAA (5)

Western blotting

Cell and exosome samples were lysed in RIPA buffer (Thermo Fisher Scientific, catalog no. 89900) supplemented with PhosSTOP (Sigma-Aldrich, catalog no. 4906837001) and Complete Mini protease inhibitors (Sigma-Aldrich, catalog no. 05892791001). Total protein concentration was measured using a bicinchoninic acid (BCA) protein assay kit (Thermo Fisher Scientific, catalog no. 23225). A total of 30 μg total protein was loaded for PC3, TRAMP-C2, and MC38 cells and exosomes, and 40 μg for CT26 and B16F10 cells and exosomes. The cell and exosome protein samples were subjected to immunoblotting by following the manufacturer recommended protocols for the antibodies used, followed by imaging using the LI-COR Odyssey 9120 imaging system.

Primary antibodies

Anti-mouse/human PVRL2 (EPR6717; Abcam, catalog no. 135246), anti-α-Tubulin (Sigma-Aldrich, catalog no. T6074), anti-Hrs (C-7; Santa Cruz Biotechnology, catalog no. sc-271455), anti-mouse/human PVRIG (EPR26274-202; Abcam, catalog no. ab307595).

Secondary antibodies

Goat anti-rabbit IgG (H+L) secondary antibody (Thermo Fisher Scientific, catalog no. 35568), goat anti-mouse IgG (H+L) secondary antibody (Thermo Fisher Scientific, catalog no. SA5-35521).

NK cell–cytotoxicity assay

NK cells were enriched from splenocytes from WT or *Pvrig* KO C57BL/6 mice by using the MojoSort Mouse NK Cell Isolation Kit (BioLegend, catalog no. 480049). Enriched NK cells were cultured and stimulated *in vitro* in RPMI1640 Medium (ATCC, catalog no. 30-2001) containing 10% FBS (Corning, ref. 35-010-CV), Penicillin/-Streptomycin (Sigma, catalog no. P4333), 1 mmol/L sodium pyruvate (GIBCO, ref. 11360-070), 0.05 mg/mL Gentamicin (GIBCO, ref. 15750-060), 2-mercaptoethanol (GIBCO, catalog no. 21985-023), supplemented with 1,000 U/mL mouse IL2 (PeproTech, catalog no. 212-12) for 7–9 days. Target cells (TRAMP-C2 WT and *Pvrl2* KO) were labeled with CellTrace Violet (Thermo Fisher Scientific, catalog no. C34557), and cocultured with WT or *Pvrig* KO NK cells as effectors at 1:1 ratio for 4 hours. Then the NK cell–mediated lysis was analyzed by flow cytometry with propidium iodide staining (Invitrogen, catalog no. P3566) according to the published protocol (42).

To generate *Pvrig*; *Tigit* and *Pvrig*; *Cd96* double KO NK cells, *Pvrig* KO NK cells were isolated from spleens of *Pvrig* KO mice and transfected with two sgRNAs targeting mouse *Tigit* or *Cd96* (IDT DNA) using Cas9-gRNA RNP-directed gene deletion on day 5. The nucleofection was conducted using a Lonza 4D-Nucleofector and a P3 Primary Cell 4D-Nucleofector X Kit S (Lonza, catalog no. V4XP-3032) with the same protocol described earlier (see *CRISPR/Cas9-mediated gene KO*). Subsequently, $TIGIT^-$ and $CD96^-$ cell populations were purified by flow-sorting on day 8. Cytotoxicity assays were performed on day 11 using the same protocol above. The sgRNA sequences were:

Mouse *Tigit* guides: CTGAAGTGACCCAAGTCGAC; TTCAGTCTTCAGTGATCGGG

Mouse *Cd96* guides: GATGACGTGTATGCTCTACC; TCCAAATCCAAGACGATGGC

Tumor models

All four mouse tumor model cell lines were cultured in their regular growth media as mentioned above (see *Cell lines*). Prior to injection, the cells were harvested by trypsinization, washed once with PBS, and then resuspended in PBS (1×10^6 cells/100 μL). A total of 1×10^6 cells per mouse were injected subcutaneously in the right flank of age matched (8–11 weeks old) male mice. Mice were considered "end stage" when the tumor volume reached 1,500 mm^3 or the tumor became ulcerated. Tumor growth was monitored every 2 or 3 days by measuring tumor length and width using caliper. Tumor volume was calculated according to the equation: $0.5 \times (\text{width})^2 \times \text{length}$.

Mouse treatments

Exosome injection

Exosomes were isolated from cultured WT and *Pvrl2* KO MC38 cells as described above (see *Exosome isolation and purification*). The exosome pellet obtained after the final centrifugation at 100,000 × *g* was resuspended in PBS (100 μL/15 cm plate), and 100 μL was injected into the tail vein of age matched (8–11 weeks old) male WT C57BL/6 mice. On the same day, 1×10^6 *Pvrl2* KO MC38 cells in 100 μL of PBS were injected subcutaneously in the right flank of the mice to establish tumors. Additional rounds of exosome isolation and injection were performed three times a week for 2 weeks.

Antibody injection

For immune-cell depletion, anti-mouse CD8α (2.43; Bio X Cell, catalog no. BE0061) and rat IgG2b isotype control (LTF-2; Bio X Cell, catalog no. BE0090) were diluted to 100 μg/100 μL with pH 7.0 dilution buffer (Bio X Cell, catalog no. IP0070); anti-mouse CD4 (GK1.5; Bio X Cell, catalog no. BE0003-1) was diluted to 200 μg/100 μL with pH 6.5 dilution buffer (Bio X Cell, catalog no. IP0065); anti-mouse NK1.1 (PK136; Bio X Cell, catalog no. BE0036) was diluted to 200 μg/100 μL with pH 7.0 dilution buffer (Bio X Cell, catalog no. IP0070). Then the antibodies were intraperitonially injected into mice (100 μL/mouse) starting one day prior to tumor injection, followed by two more weekly doses. For TIGIT blockade, anti-mouse TIGIT (1B4; Absolute Antibody, catalog no. Ab01258-1.1) or mouse IgG1 isotype control (MOPC-21; Bio X Cell, catalog no. BE0083) were intraperitoneally injected into mice starting on day 4 after tumor injection followed by a serial four doses (200 μg/mouse) every 3 days, and a maintenance dose (100 μg/mouse) on day 20.

Immune profiling

Age-matched and randomly assigned male C57BL/6 mice were implanted subcutaneously with 1×10^6 MC38 WT or *Pvrl2* KO cells to the right flank. On day 25, mice were euthanized, and tumors surgically removed with sterilized surgical equipment, weighed, and minced into small pieces using scissors. The minced tumor tissue was transferred to a 6-well plate containing 3 mL/well of tumor digestion media [NK cell media + 1 mg/mL collagenase IV (Sigma, catalog no. C5138) + 0.2 mg/mL DNAse I (Roche, catalog no. 10104159001)] and incubated on a shaker at 37°C for 1 hour. Cell mixtures were then filtered through a 70 μm strainer into 50 mL conical tubes. Cells were then washed once with FACS buffer [PBS + 2% heat inactivated FBS + 1 mmol/L Ethylenediaminetetraacetic Acid (EDTA)] and counted. $CD45^+$ cells were enriched using the EasySep Mouse TIL (CD45) positive selection kit (STEMCELL, catalog no. 100-0350) according to the manufacturer's protocol.

Single-cell suspensions (1×10^6 cells) were first stained with cell viability dye (1:1,000 in PBS; eBioscience, catalog no. 65-0866-14; CYTEK, catalog no. SKU 13-0865-T100) for 30 minutes at 4°C in dark to exclude dead cells. After two washes with FACS buffer, cells were incubated with Fc Block (Tombo Biosciences, catalog no. 70-0161) for 10 minutes and then coincubated with fluorescently labeled antibodies for 30 minutes at 4°C in dark, followed by three washes with FACS buffer. Detailed information of the flow cytometry antibodies used in this study are listed below. Flow cytometry was performed on LSRII S854-S864, and data were analyzed by FlowJo 10.8.1.

Flow antibodies:

Anti-mouse CD8 Brilliant Violet 605 (53-6.7; BioLegend, catalog no. 100744),

anti-mouse CD4 Brilliant Violet 421 (GK1.5; BioLegend, catalog no. 100437),

anti-mouse NK1.1 PE (PK136; BioLegend, catalog no. 108707),

anti-mouse NK1.1 Brilliant Violet 711 (PK136; BioLegend, catalog no. 108745),

anti-mouse CD107a (LAMP-1) Brilliant Violet 711 (1D4B; BioLegend, catalog no. 121631),

anti-mouse PD-1 (CD279) APC (J43; BD Biosciences, catalog no. 562671),

anti-mouse PVRL2 Brilliant Violet 421 (BD Biosciences, catalog no. 748046),

anti-mouse PVR PE (TX56; BioLegend, catalog no. 131507),

anti-mouse PVR APC (TX56; BioLegend, catalog no. 131509),

anti-mouse TIGIT PE (1G9; BioLegend, catalog no. 142104),

anti-mouse CD96 APC (3.3; BioLegend, catalog no. 131711),

anti-mouse DNAM-1 Brilliant Violet 785 (TX42.1; BioLegend, catalog no. 133611),

anti-mouse CD98 PE (4F2; BioLegend, catalog no. 128207),

anti-mouse PD-L1 Super Bright 780 (MIH5; Invitrogen, catalog no. 78-5982-82),

Brilliant Violet 605 Rat IgG2a, k Isotype control (RTK2758; BioLegend, catalog no. 400539),

Brilliant Violet 421 Rat IgG2b, κ Isotype control (RTK4530; BioLegend, catalog no. 400639),

PE Mouse IgG2a, κ Isotype control (MOPC-173; BioLegend, catalog no. 400211),

Brilliant Violet 711 Rat IgG2b, κ Isotype control (RTK4530; BioLegend, catalog no. 400653),

APC Hamster IgG2, κ Isotype control (B81-3; BD Biosciences, catalog no. 562169).

Immunofluorescence and image analysis

Age-matched and randomly assigned male C57BL/6 mice were implanted subcutaneously with 1×10^6 MC38 WT or *Pvrl2* KO cells. On day 25 or 27, mice were euthanized, and tumors dissected and

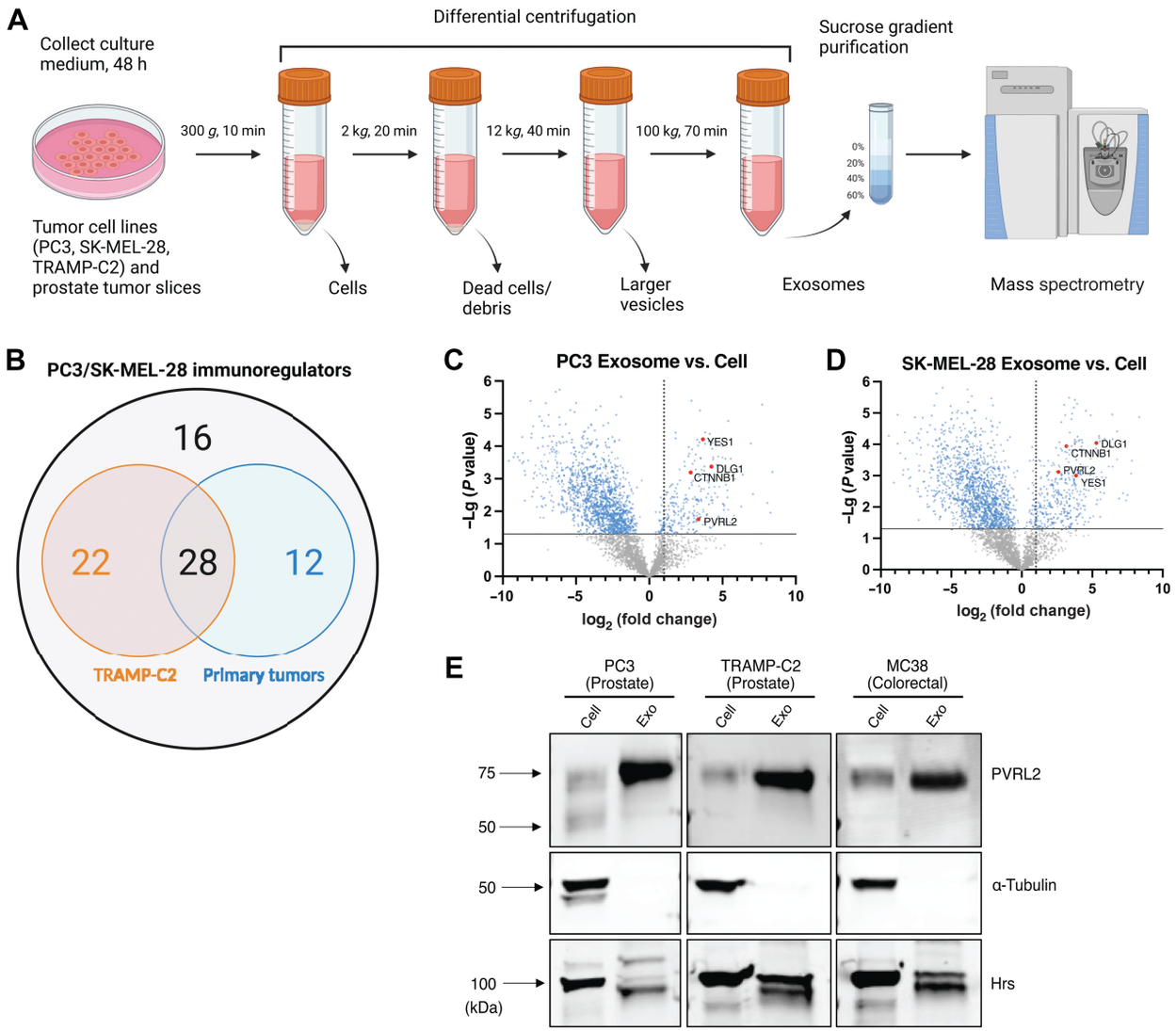

Figure 1.

Proteomic analysis identifies PVRL2 on tumor-derived exosomes. **A,** Schematic of exosome collection: exosomes were collected from the indicated tumor cell lines and primary tumor slices via differential centrifugations and purified by sucrose gradient. Exosomes and cells were then lysed, and their respective proteomes were analyzed by mass spectrometry. **B,** The numbers of shared immunoregulatory molecules identified from mass spectrometry results of the exosomes from the indicated tumor cell lines and primary tumors. Volcano plots present protein abundance differences in exosomes over in cells in PC3 (**C**) and SK-MEL-28 (**D**) cell lines as determined by label free quantitation. Proteins on the right of the volcano plot represent proteins enriched in exosomes versus cells. Proteins with a $\log_2$ (fold change) value > 1 are over 2-fold enriched. **E,** Western blot analysis for PVRL2 in the cells and exosomes (exo) from the indicated tumor cell lines. A total of 30 μg of total protein was loaded for each sample. α-Tubulin was used as the loading control for cells, and Hrs as the loading control for exosomes.

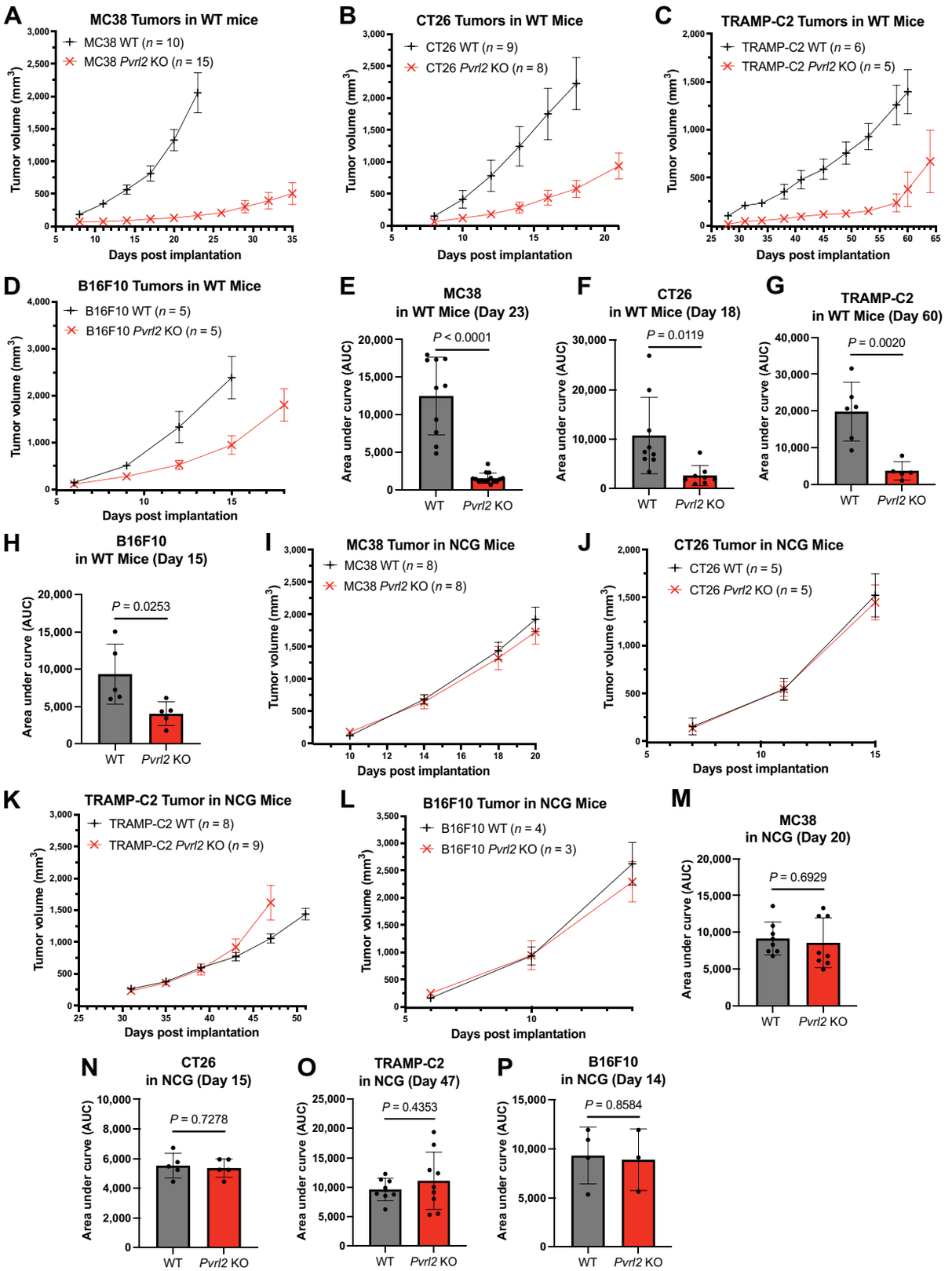
A
MC38 Tumors in WT mice
MC38 WT (n = 10)
MC38 Pvrl2 KO (n = 15)
Tumor volume (mm3)
Days post implantation
B
CT26 Tumors in WT Mice
CT26 WT (n = 9)
CT26 Pvrl2 KO (n = 8)
Tumor volume (mm3)
Days post implantation
C
TRAMP-C2 Tumors in WT Mice
TRAMP-C2 WT (n = 6)
TRAMP-C2 Pvrl2 KO (n = 5)
Tumor volume (mm3)
Days post implantation
D
B16F10 Tumors in WT Mice
B16F10 WT (n = 5)
B16F10 Pvrl2 KO (n = 5)
Tumor volume (mm3)
Days post implantation
E
MC38
in WT Mice (Day 23)
P < 0.0001
Area under curve (AUC)
WT
Pvrl2 KO
F
CT26
in WT Mice (Day 18)
P = 0.0119
Area under curve (AUC)
WT
Pvrl2 KO
G
TRAMP-C2
in WT Mice (Day 60)
P = 0.0020
Area under curve (AUC)
WT
Pvrl2 KO
H
B16F10
in WT Mice (Day 15)
P = 0.0253
Area under curve (AUC)
WT
Pvrl2 KO
I
MC38 Tumor in NCG Mice
MC38 WT (n = 8)
MC38 Pvrl2 KO (n = 8)
Tumor volume (mm3)
Days post implantation
J
CT26 Tumor in NCG Mice
CT26 WT (n = 5)
CT26 Pvrl2 KO (n = 5)
Tumor volume (mm3)
Days post implantation
K
TRAMP-C2 Tumor in NCG Mice
TRAMP-C2 WT (n = 8)
TRAMP-C2 Pvrl2 KO (n = 9)
Tumor volume (mm3)
Days post implantation
L
B16F10 Tumor in NCG Mice
B16F10 WT (n = 4)
B16F10 Pvrl2 KO (n = 3)
Tumor volume (mm3)
Days post implantation
M
MC38
in NCG (Day 20)
P = 0.6929
Area under curve (AUC)
WT
Pvrl2 KO
N
CT26
in NCG (Day 15)
P = 0.7278
Area under curve (AUC)
WT
Pvrl2 KO
O
TRAMP-C2
in NCG (Day 47)
P = 0.4353
Area under curve (AUC)
WT
Pvrl2 KO
P
B16F10
in NCG (Day 14)
P = 0.8584
Area under curve (AUC)
WT
Pvrl2 KO

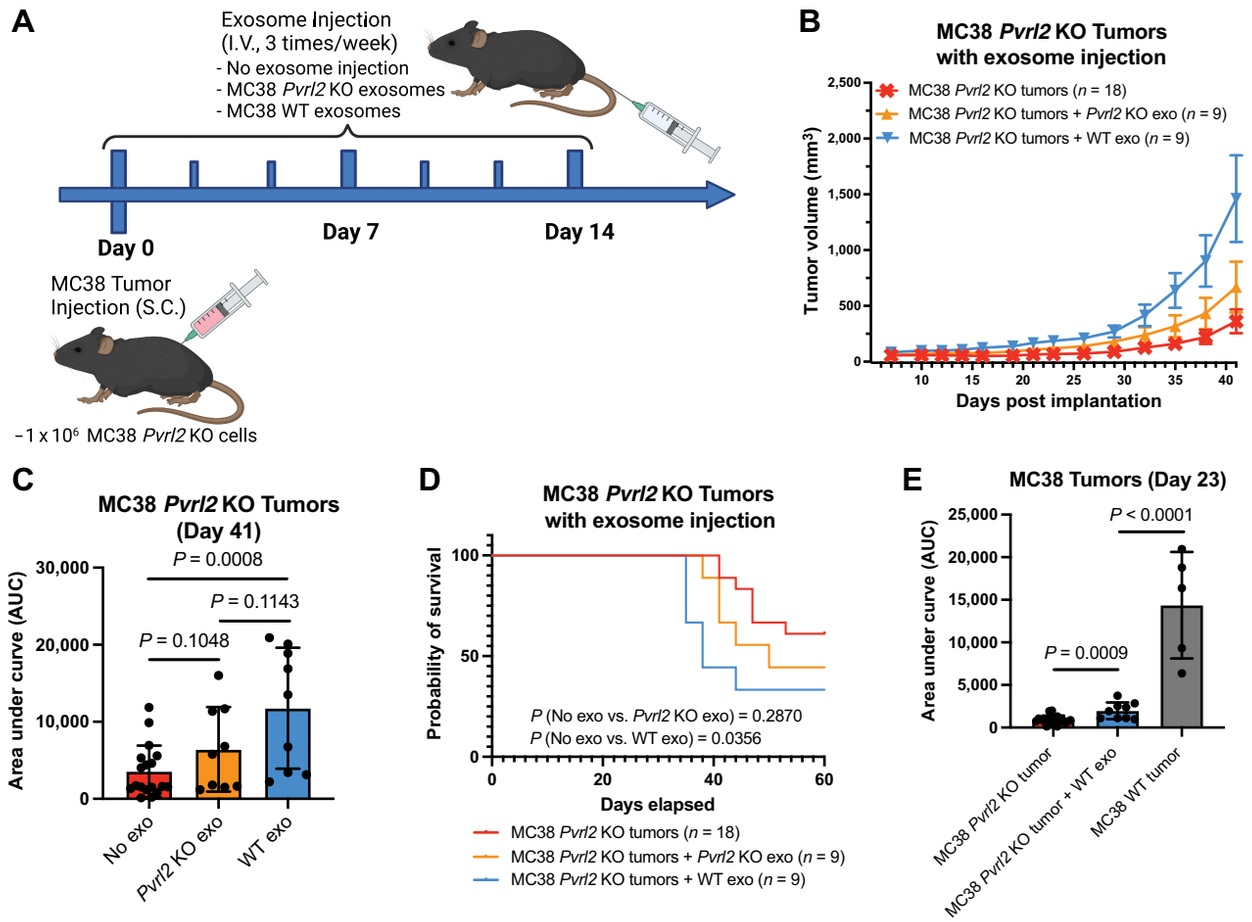

Figure 3.

Exosomal PVRL2 partially rescues the phenotype of *Pvrl2* KO tumors. **A,** Schematic of the experiment: 1×10^6 MC38 *Pvrl2* KO cells were injected into C57BL/6 mice, and starting from the same day, exosomes collected from MC38 WT and *Pvrl2* KO cells were injected into the mice through tail vein according to the indicated timeline. **B,** Average tumor volume over time following the injection of MC38 *Pvrl2* KO tumors along with no exosome injection, MC38 WT exosomes, and MC38 *Pvrl2* KO exosomes as indicated in **A**. Error bars represent SEM. **C,** AUCs of the tumor growth in **B** on day 41. Dots represent individual mice. *P* values are calculated by unpaired *t* test. Error bars represent SD. **D,** Mouse survival curves following injections as described in **B**. *P* values are calculated by log-rank test. **E,** AUCs of the growth of MC38 *Pvrl2* KO tumors with no exosome injection or WT exosome injection from **B**, in comparison with the MC38 WT tumors from **Fig. 2A** on day 23. Dots represent individual mice. *P* values are calculated by unpaired *t* test. Error bars represent SD.

rinsed with PBS. Tumors were fixed in 10% neutral buffered formalin at room temperature overnight, after which they were dehydrated by sucrose (5% for 1 hour, 10% for 1 hour, 20% overnight) and embedded in Scigen Tissue-Plus O.C.T. Compound (Thermo Fisher Scientific, catalog no. 23-730-571).

For immunofluorescence (IF), tumors were sectioned into 10 μm slides using a Leica CM 3050S cryostat. Sections were rehydrated with PBS for 10 minutes. Antigen retrieval was performed using EDTA antigen retrieval buffer (10 mmol/L Tris base, 1 mmol/L EDTA solution, 0.05% Tween 20, pH∼9) in a steamer for 20 minutes. Sections were incubated in blocking buffer (PBS with 1% BSA and 5% donkey serum) at room temperature for 1 hour before overnight incubation with primary antibodies diluted 1:100 in blocking buffer at 4°C. Anti-CD8a (Invitrogen, catalog no. 14-0808-80; 1:100) and anti-NCR1 (Abcam, catalog no. ab233558; 1:100) primary antibodies were used. After primary antibody incubation, sections were washed with Tris-buffered saline (TBS) with 0.05% Tween-20 detergent and then incubated with DAPI (Invitrogen, catalog no. D1306;

Figure 2.

PVRL2 promotes tumor growth through an immune-dependent mechanism. Average tumor volume over time following subcutaneous injection of 1×10^6 WT or *Pvrl2* KO MC38 (**A**), TRAMP-C2 (**C**), and B16F10 (**D**) cells in C57BL/6 mice, and CT26 (**B**) in BALB/cJ mice. Error bars represent SEM. AUCs of the MC38 (**E**), CT26 (**F**), TRAMP-C2 (**G**), and B16F10 (**H**) tumors from **A**–**D** calculated at day when the first mouse reached endpoint: day 23, 18, 60, and 15, respectively. Dots represent individual mice. *P* values are calculated by unpaired *t* test. Error bars represent SD. Average tumor volume over time following subcutaneous injection of 1×10^6 MC38 (**I**), CT26 (**J**), TRAMP-C2 (**K**), and B16F10 (**L**) WT and *Pvrl2* KO cells in NCG mice. Error bars represent SEM. AUCs of the MC38 (**M**), CT26 (**N**), TRAMP-C2 (**O**), and B16F10 (**P**) tumors from **I**–**L** calculated at day when the first mouse reached endpoint: day 20, 15, 47, and 14, respectively. Dots represent individual mice. *P* values are calculated by unpaired *t* test. Error bars represent SD.

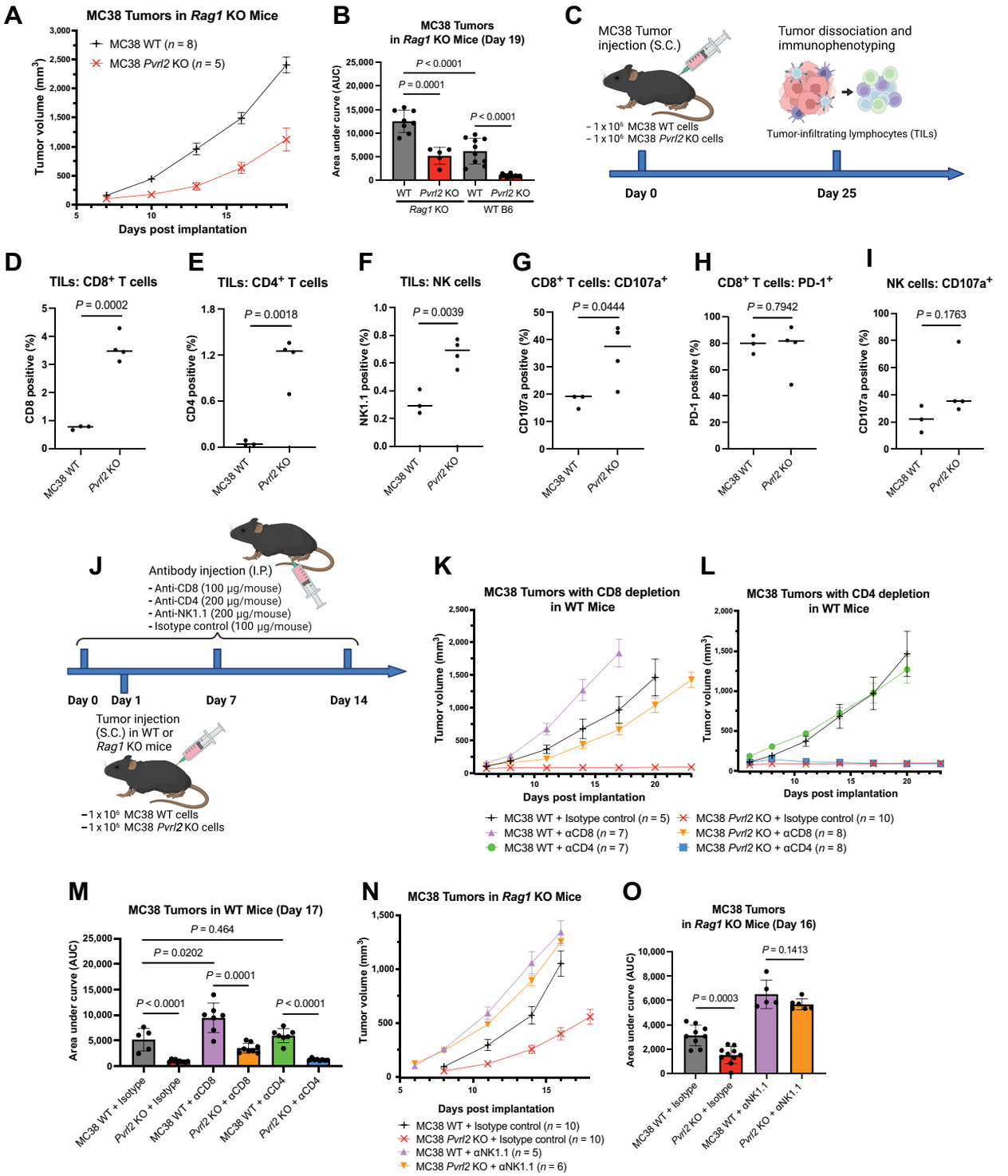

Figure 4.

PVRL2 regulates CD8 T-cell and NK-cell activation. **A,** Average tumor volume over time following subcutaneous injection of 1×10^6 WT and *Pvrl2* KO MC38 cells in *Rag1* KO mice. Error bars represent SEM. **B,** AUCs of the MC38 tumors from **A** and **Fig. 2A** on day 19. Dots represent individual mice. *P* values are calculated by unpaired *t* test. Error bars represent SD. **C,** Schematic of immunophenotyping experiment: 25 days after subcutaneous injection of 1×10^6 MC38 WT and *Pvrl2* KO cells in C57BL/6 mice, the tumors were collected. $CD45^+$ cell populations were isolated from the tumor dissociates using CD45 positive magnetic selection kit. Then the isolated cells were subjected to viability dye, CD8, CD4, NK1.1, CD107a, and PD-1 staining followed by flow cytometry analysis. (*Continued on the following page.*)

1:1,000) and fluorescence-conjugated secondary antibodies diluted 1:200 in blocking buffer for 1 hour at room temperature. Donkey anti-Rat IgG (H+L) Alexa Fluor 488 (Invitrogen, catalog no. A21208) and Goat anti-Rabbit IgG (H+L) Alexa Fluor 594 (Invitrogen, catalog no. A11012) were used for CD8a and NCR1 staining, respectively. Sections were washed with TBST and mounted using the ProLong Gold Antifade Mountant (Invitrogen, catalog no. P36930). Images were acquired using a Leica SP8 confocal microscope. All images were processed with ImageJ 1.53.

A 3–6 μm z-stack with system optimized step-size was taken for each field of view. To quantify the total number of $CD8^+$ T cells and NK cells in each z-stack of field of view, maximum intensity projection was applied to all slices in the z-stack. $CD8^+$ T cells and NK cells were then counted manually. A representative slice in the z-stack was shown.

Statistical analysis

All statistical analyses were processed with GraphPad Prism, Version 9.4.1 (GraphPad). Statistical significance between groups of AUC of tumor growth, *in vitro* NK cell–cytotoxicity assays, immune profiling, and IF images were calculated using unpaired Student *t* test. Statistical significance for mouse survival was analyzed by log-rank test. No statistical method was used to predetermine sample size. No datapoints were excluded from the analyses of all experiments. In all cases, significance was defined by a *P* value of 0.05 and below. Details regarding the *P* values, number of replicates and the definition of center and error bars are indicated in figures and figure legends. *P* values for AUC comparisons not shown in the figures can be found in Supplementary Table S1.

Data and material availability

The mass spectrometry proteomics data that support the findings of this study have been deposited to the ProteomeXchange Consortium via the PRIDE (43) partner repository with the dataset identifier PXD044245. All the remaining data that support the conclusions from this study are included in this article and its Supplementary Data files or are available from the corresponding author on reasonable request. *Pvrl2* and *Pvr* KO tumor cell lines and *Pvrig* KO mice generated in this study will be made available on request with completed Material Transfer Agreements.

Results

Proteomic analysis identifies PVRL2 on tumor-derived exosomes

To identify immunosuppressive molecules beyond PD-L1 that are present on tumor-derived exosomes, we employed mass spectrometry–based proteomic analysis of exosomes isolated from two human cancer cell lines, PC3 (prostate cancer) and SK-MEL-28 (melanoma; **Fig. 1A**). The analysis revealed over 2,000 proteins on PC3 and SK-MEL-28 exosomes, including 78 proteins identified as regulators of immune responses, as determined by functional gene enrichment analysis (Supplementary Fig. S1A). We extended our proteomic analysis to the mouse prostate cancer cell line TRAMP-C2 and two *ex vivo* cultured primary human prostate cancer tumor slices (**Fig. 1A**). Among the list of 78 immune regulators from analysis of PC3 and SK-MEL-28 exosomes, 28 proteins were also detected in at least one sample derived from TRAMP-C2 and primary tumor exosomes (**Fig. 1B**; Supplementary Fig. S1B). We looked for proteins enriched on exosomes relative to their cell of origin, uncovering 274 proteins from PC3 and 405 proteins from SK-MEL-28 exosomes including four out of the 28 shared immunoregulators that were significantly enriched in the PC3 and SK-MEL-28 exosomes relative to the cells (>2-fold, $P < 0.05$; **Fig. 1C** and **D**; Supplementary Fig. S1C). These four proteins were DLG1, YES1, PVRL2, and CTNNB1 (**Fig. 1C** and **D**; Supplementary Fig. S1C). We focused on PVRL2 given its previously reported immunoregulatory functions (14, 18, 25, 44). To validate and expand on our proteomic data, we performed immunoblot analysis for PVRL2 on TRAMP-C2 and PC3 cell and exosome fractions as well as three other mouse tumor cell lines, two colorectal cell lines (MC38 and CT26) and a melanoma cell line (B16F10). All five lines showed robust levels of PVRL2 protein in both cells and exosomes (**Fig. 1E**; Supplementary Fig. S1D). These data uncover the presence of PVRL2 in both the cellular and exosomal fractions of multiple mouse and human tumor cells representing different cancer types.

PVRL2 promotes tumor growth through an immune-dependent mechanism

Given the presence of PVRL2 on both tumor exosomes and cells, we performed functional experiments in mice to test the relevance of PVRL2 in the regulation of antitumor immune responses. We used CRISPR/Cas9-directed mutagenesis to knock out *Pvrl2* (gene encoding PVRL2, also known as *Nectin2*) in the four mouse syngeneic tumor cell lines (Supplementary Fig. S2A). Flow cytometry analysis confirmed loss of the PVRL2 protein in the mutant clones of each line (Supplementary Fig. S2B–S2E). *In vitro* growth analysis showed no effect of PVRL2 loss on the tumor cell growth rate *in vitro* (Supplementary Fig. S2F–S2I). The mutant cell lines were transplanted into immunocompetent isogenic mice (C57BL/6 for MC38, TRAMP-C2, and B16F10; BALB/cJ for CT26). In all four models, PVRL2 loss led to a dramatic reduction in tumor growth and extended the survival of the mice (**Fig. 2A–H**; Supplementary Fig. S2J–S2M). Comparison with a *Pdl1* KO in the MC38 model showed an even greater impact on tumor growth with PVRL2 loss than with PD-L1 loss (Supplementary Fig. S2N–S2Q). To determine whether the PVRL2 effects were specifically through the regulation of the immune response, we repeated the experiments in NCG mice, which are deficient for T, B, and NK cells and have reduced macrophage and dendritic cell function (45–47).

(*Continued.*) Flow cytometric quantification of the percentage of $CD8^+$ (**D**), $CD4^+$ (**E**), and $NK1.1^+CD8^-$ (NK cells; **F**) populations, respectively, in the $CD45^+$ cells isolated from the MC38 WT ($n = 3$) and *Pvrl2* KO ($n = 4$) tumors as indicated in **C**. *P* values are calculated by unpaired *t* test. Line represents mean. Quantification of the percentage of $CD107a^+$ (**G**) and PD-1^+ (**H**) cells among the $CD8^+$ T cell (**D**) population. *P* values are calculated by unpaired *t* test. Line represents mean. **I,** Quantification of the percentage of $CD107a^+$ cells among the NK cell (**F**) population. *P* value is calculated by unpaired *t* test. Line represents mean. **J,** Schematic of experiment design in **K–O**: After subcutaneous injection of 1×10^6 MC38 WT and *Pvrl2* KO cells in C57BL/6 WT or *Rag1* KO mice, the mice were treated with anti-CD8, CD4, or NK1.1 depleting antibodies or isotype control at the indicated serial doses and schedule. Average tumor volume over time following subcutaneous injection of 1×10^6 MC38 WT and *Pvrl2* KO cells in WT C57BL/6 mice with anti-CD8 (**K**) and anti-CD4 (**L**) depleting antibodies or isotype control as indicated in **J**. Error bars represent SEM. **M,** AUCs of the MC38 tumors from (**K**) and (**L**) on day 17. Dots represent individual mice. *P* values are calculated by unpaired *t* test. Error bars represent SD. **N,** Average tumor volume over time following subcutaneous injection of 1×10^6 MC38 WT and *Pvrl2* KO cells in *Rag1* KO mice with anti-NK1.1 depleting antibody or isotype control as indicated in **J**. Error bars represent SEM. **O,** AUCs of the MC38 tumors from **N** on day 16. Dots represent individual mice. *P* values are calculated by unpaired *t* test. Error bars represent SD.

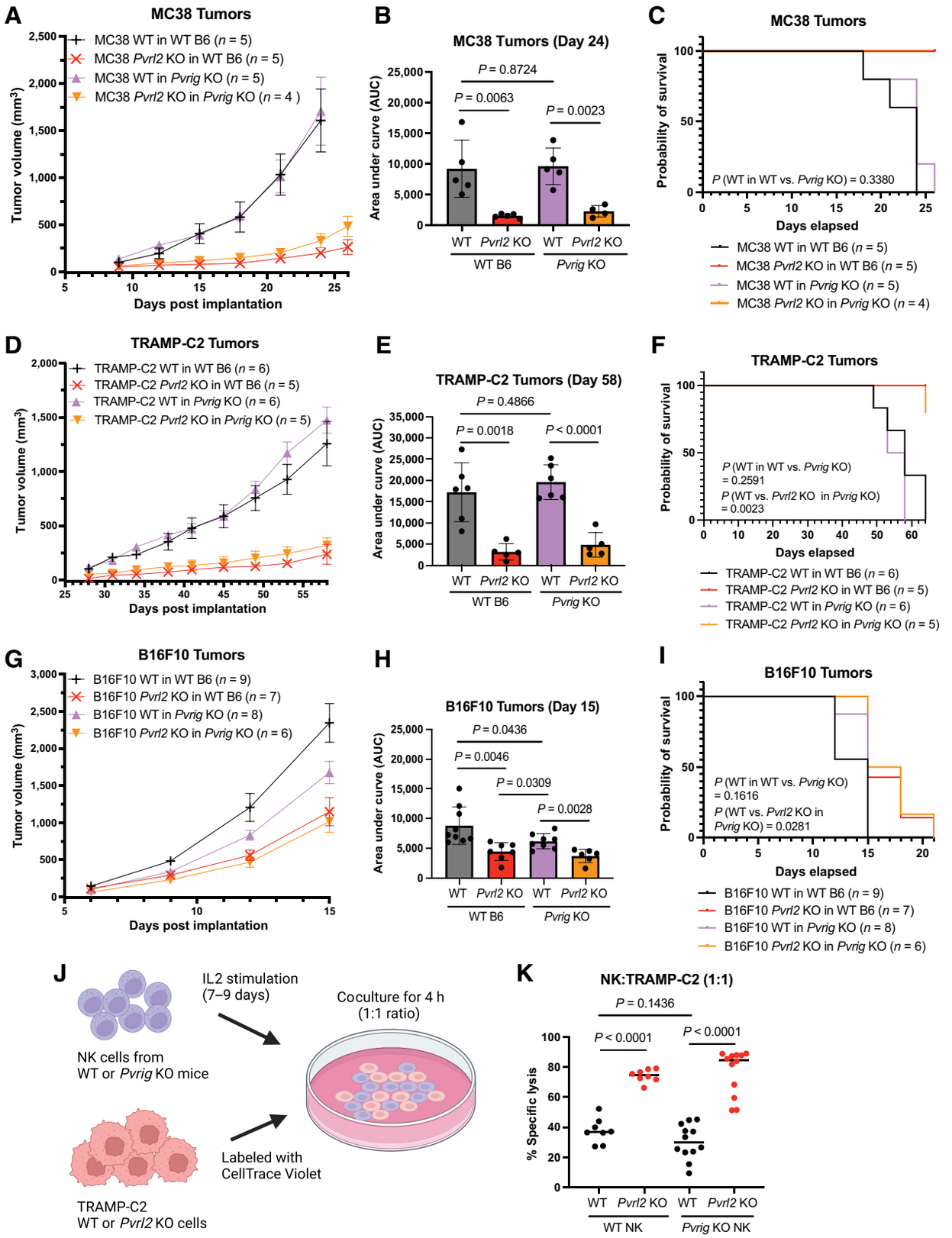
A
MC38 Tumors
MC38 WT in WT B6 (n = 5)
MC38 Pvrl2 KO in WT B6 (n = 5)
MC38 WT in Pvrig KO (n = 5)
MC38 Pvrl2 KO in Pvrig KO (n = 4)
Tumor volume (mm3)
Days post implantation
B
MC38 Tumors (Day 24)
P = 0.8724
P = 0.0063
P = 0.0023
Area under curve (AUC)
WT Pvrl2 KO WT Pvrl2 KO
WT B6
Pvrig KO
C
MC38 Tumors
Probability of survival
P (WT in WT vs. Pvrig KO) = 0.3380
Days elapsed
MC38 WT in WT B6 (n = 5)
MC38 Pvrl2 KO in WT B6 (n = 5)
MC38 WT in Pvrig KO (n = 5)
MC38 Pvrl2 KO in Pvrig KO (n = 4)
D
TRAMP-C2 Tumors
TRAMP-C2 WT in WT B6 (n = 6)
TRAMP-C2 Pvrl2 KO in WT B6 (n = 5)
TRAMP-C2 WT in Pvrig KO (n = 6)
TRAMP-C2 Pvrl2 KO in Pvrig KO (n = 5)
Tumor volume (mm3)
Days post implantation
E
TRAMP-C2 Tumors (Day 58)
P = 0.4866
P = 0.0018
P < 0.0001
Area under curve (AUC)
WT Pvrl2 KO WT Pvrl2 KO
WT B6
Pvrig KO
F
TRAMP-C2 Tumors
Probability of survival
P (WT in WT vs. Pvrig KO) = 0.2591
P (WT vs. Pvrl2 KO in Pvrig KO) = 0.0023
Days elapsed
TRAMP-C2 WT in WT B6 (n = 6)
TRAMP-C2 Pvrl2 KO in WT B6 (n = 5)
TRAMP-C2 WT in Pvrig KO (n = 6)
TRAMP-C2 Pvrl2 KO in Pvrig KO (n = 5)
G
B16F10 Tumors
B16F10 WT in WT B6 (n = 9)
B16F10 Pvrl2 KO in WT B6 (n = 7)
B16F10 WT in Pvrig KO (n = 8)
B16F10 Pvrl2 KO in Pvrig KO (n = 6)
Tumor volume (mm3)
Days post implantation
H
B16F10 Tumors (Day 15)
P = 0.0436
P = 0.0046
P = 0.0309
P = 0.0028
Area under curve (AUC)
WT Pvrl2 KO WT Pvrl2 KO
WT B6
Pvrig KO
I
B16F10 Tumors
Probability of survival
P (WT in WT vs. Pvrig KO) = 0.1616
P (WT vs. Pvrl2 KO in Pvrig KO) = 0.0281
Days elapsed
B16F10 WT in WT B6 (n = 9)
B16F10 Pvrl2 KO in WT B6 (n = 7)
B16F10 WT in Pvrig KO (n = 8)
B16F10 Pvrl2 KO in Pvrig KO (n = 6)
J
IL2 stimulation (7–9 days)
Coculture for 4 h (1:1 ratio)
NK cells from WT or Pvrig KO mice
Labeled with CellTrace Violet
TRAMP-C2 WT or Pvrl2 KO cells
K
NK:TRAMP-C2 (1:1)
P = 0.1436
P < 0.0001
P < 0.0001
% Specific lysis
WT Pvrl2 KO WT Pvrl2 KO
WT NK
Pvrig KO NK

In this background, the WT and *Pvrl2* KO tumors grew equally fast resulting in the rapid demise of their hosts (**Fig. 2I**-**P**). Together, these results identify PVRL2 as a key promoter of tumor growth *in vivo*, functioning through an immune-dependent mechanism.

Exosomal PVRL2 partially rescues the phenotype of *Pvrl2* KO tumors

We addressed whether and to what degree PVRL2 secreted in exosomes contributes to the overall ability of PVRL2 to promote tumor growth. To address this question, we focused on the rapidly growing MC38 model. *Pvrl2* KO MC38 cells were transplanted into WT C57BL/6 mice. Exosomes were isolated from cultured WT and *Pvrl2* KO MC38 cells. These exosomes were injected into the tail vein of the mice starting on the same day as tumor cell transplantation and continued three times per week for 2 weeks (**Fig. 3A**). The injection of exosomes from the WT cells significantly accelerated the growth of *Pvrl2* KO tumors and reduced the survival of the treated mice (**Fig. 3B**–**D**). However, growth remained well below that of transplanted WT cells (**Fig. 3E**). In contrast, *Pvrl2* KO exosomes did not significantly impact tumor growth or mouse survival (**Fig. 3B**–**D**). These findings show that exosomal PVRL2 can act to partially rescue growth of *Pvrl2* KO tumor cells. However, the contribution of exosomal PVRL2 to promoting tumor growth appears small relative to that of cellular PVRL2.

PVRL2 regulates $CD8^+$ T-cell and NK-cell activation

The PVRL2 receptor PVRIG is expressed on T cells and NK cells (48), and has been shown to display immune inhibitory function on these cells in both mouse and human models (19, 24, 25, 49–51). However, there is currently no direct evidence showing that PVRL2 regulates these specific cell populations. Therefore, we set out to resolve what immune populations were impacted and responsible for PVRL2's role in promoting tumor growth. First, to determine whether PVRL2 primarily functions through adaptive or innate immunity, we transplanted MC38 tumor cells into *Rag1* KO mice, which lack functional T and B cells and thus lack the adaptive immune response. Even in the absence of adaptive immunity, MC38 WT tumors maintained significantly faster growth than *Pvrl2* KO tumors, indicating that the remaining innate immune response plays a crucial role in PVRL2 function (**Fig. 4A** and **B**). However, the ratios of WT over KO tumor size and the AUCs were reduced in the *Rag1* KO mice supporting a role of the adaptive response as well (Supplementary Fig. S3A).

To understand which specific immune populations were responsible for the regulation of adaptive and innate immunity by PVRL2, we performed immune profiling of the tumor microenvironment by flow cytometry (**Fig. 4C**). Isolated $CD45^+$ cells from MC38 WT and *Pvrl2* KO tumors were stained with a viability dye and antibodies against CD8, CD4, NK1.1, and the activation markers CD107a and PD-1 (Supplementary Fig. S3B–S3D). *Pvrl2* KO tumors had significantly higher fractions of $CD8^+$ T cells, $CD4^+$ T cells, and NK cells (**Fig. 4D**–**F**). Furthermore, a significantly larger proportion of $CD8^+$ T cells expressed the degranulation marker CD107a in *Pvrl2* KO tumors, indicating enhanced activation of these cells (**Fig. 4G**; Supplementary Fig. S3C). In contrast, PD-1 was unchanged (**Fig. 4H**; Supplementary Fig. S3D). NK cells in *Pvrl2* KO tumors also exhibited slightly higher CD107a positivity, although the data did not reach statistical significance (**Fig. 4I**). These findings show that *Pvrl2* KO promotes the infiltration and activation of adaptive and innate immune cells. IF staining of the tumor sections confirmed the increased infiltration of $CD8^+$ T cells and NK cells in MC38 *Pvrl2* KO tumors compared with WT tumors (Supplementary Fig. S3E–S3H).

To further validate that the function of PVRL2 is dependent on T cells and NK cells *in vivo*, we depleted these specific cell populations with antibodies to CD8, CD4, or NK1.1 (**Fig. 4J**). Depletion of $CD8^+$ T cells resulted in a significant promotion of both MC38 *Pvrl2* KO and WT tumor growth (**Fig. 4K** and **M**) and extended the survival of the mice (Supplementary Fig. S3J). Although the WT tumors still exhibited significantly faster growth than *Pvrl2* KO tumors, the difference between WT and *Pvrl2* KO tumors became smaller upon $CD8^+$ T-cell depletion, as indicated by the ratio of WT tumor over *Pvrl2* KO tumor size and the AUC (Supplementary Fig. S3I). In contrast, $CD4^+$ T-cell depletion did not impact tumor growth or survival (**Fig. 4L** and **M**; Supplementary Fig. S3J). To specifically measure the contribution of NK cells, we depleted NK cells in the *Rag1* KO background. This led to the abolishment of any differences between MC38 *Pvrl2* KO and WT tumor growth and mouse survival (**Fig. 4N** and **O**; Supplementary Fig. S3K). Together, these results show that PVRL2 on tumor cells suppresses both adaptive and innate immune responses and does so through inhibition of $CD8^+$ T and NK cells, respectively.

PVRL2 functions through a PVRIG-independent mechanism

As PVRL2 has been shown to bind to the coinhibitory receptor PVRIG, it is assumed that PVRIG underlies PVRL2 function in the suppression of antitumor immune response (19, 25, 49–51). However, no evidence exists indicating whether PVRL2 directly regulates PVRIG. Our data show a much greater effect of PVRL2 loss on tumor growth than previously published for PVRIG loss or antibody blockade (24, 51). To ask whether PVRIG is indeed the primary receptor responsible for mediating the ability of PVRL2 to promote tumor growth, we produced *Pvrig* KO mice using sperm from the KOMP. The KO involves a

Figure 5.

PVRL2 functions through a PVRIG independent mechanism. **A,** Average tumor volume over time following subcutaneous injection of 1×10^6 MC38 WT and *Pvrl2* KO cells in WT C57BL/6 mice and *Pvrig* KO mice. Error bars represent SEM. **B,** AUCs of the MC38 tumors from **A** on day 24. Dots represent individual mice. *P* values are calculated by unpaired *t* test. Error bars represent SD. **C,** Mouse survival curves following subcutaneous injections as described in **A**. *P* values are calculated by log rank test. **D,** Average tumor volume over time following subcutaneous injection of 1×10^6 TRAMP-C2 WT and *Pvrl2* KO cells in WT C57BL/6 and *Pvrig* KO mice. Error bars represent SEM. **E,** AUCs of the TRAMP-C2 tumors from **D** on day 58. Dots represent individual mice. *P* values are calculated by unpaired *t* test. Error bars represent SD. **F,** Mouse survival curves following injections as described in **D**. *P* values are calculated by log-rank test. **G,** Average tumor volume over time following subcutaneous injection of 1×10^6 B16F10 WT and *Pvrl2* KO cells in WT C57BL/6 mice and *Pvrig* KO mice. Error bars represent SEM. **H,** AUCs of the B16F10 tumors from **G** on day 15. Dots represent individual mice. *P* values are calculated by unpaired *t* test. Error bars represent SD. **I,** Mouse survival curves following subcutaneous injections as described in **G**. *P* values are calculated by log-rank test. **J,** Schematic of experiment design in **K**: NK cells were isolated from WT C57BL/6 or *Pvrig* KO mice. After 7–9 days *in vitro* stimulation with IL2, NK cells were cocultured at 1:1 TRAMP WT or *Pvrl2* KO tumor cells for 4 hours. Then NK cell lysis was evaluated by live/dead cell dye followed by flow cytometry. **K,** Percentage lysis of TRAMP-C2 WT and *Pvrl2* KO cells after coculturing with WT or *Pvrig* KO NK cells at 1:1 ratio. Dots represent individual replicates. 4 replicates per condition in each experiment ($n = 2$ and $n = 3$ independent experiments for WT NK cells and *Pvrig* KO NK cells, respectively). *P* values are calculated by unpaired *t* test. Line represents mean.

deletion spanning exons 1 through 4 plus part of 5, which removes the entire coding region of *Pvrig* in a C57BL/6 background (Supplementary Fig. S4A). Genotyping by PCR validated the loss of *Pvrig* (Supplementary Fig. S4A–S4C). Furthermore, Western blot analysis confirmed the depletion of PVRIG protein in the splenocytes from *Pvrig* KO mice (Supplementary Fig. S4D). All three WT and *Pvrl2* KO C57BL/6 mouse syngeneic mouse models (MC38, TRAMP-C2, and B16F10) were then transplanted into the mice. The removal of PVRIG did not influence the growth or survival of WT MC38 tumors (**Fig. 5A–C**). Furthermore, the removal of PVRL2 was equally effective in both inhibiting MC38 tumor growth and enhancing survival in WT and *Pvrig* KO backgrounds (**Fig. 5A–C**). This effect cannot be ascribed to the indirect regulation of other Nectin family immunoregulatory receptors, including TIGIT, DNAM-1, and CD96, as the loss of PVRIG in mice did not lead to significant alterations in the expression of these receptors on $CD8^+$ T cells and NK cells (Supplementary Fig. S4E and S4F). Similar results were observed with the TRAMP-C2 model, where PVRIG loss had no impact on the growth of WT or *Pvrl2* KO tumors (**Fig. 5D–F**). However, in the B16F10 model, the loss of PVRIG resulted in a notable, albeit partial, decrease in tumor growth (**Fig. 5G** and **H**); survival showed a trend toward improvement, but was not statistically significant (**Fig. 5I**). Moreover, in all three tumor models (MC38, TRAMP-C2, and B16F10), the loss of PVRL2 alone had a greater impact compared with PVRIG loss alone, and PVRL2 loss further reduced tumor growth in a *Pvrig* KO background (**Fig. 5G** and **H**). In contrast, the growth of *Pvrl2* KO tumors was not additionally affected in the *Pvrig* KO background across all three cell lines (**Fig. 5A–I**). These data show that PVRL2 functions beyond PVRIG in promoting tumor growth.

To confirm that the PVRIG-independent role for PVRL2 in promoting tumor growth is through the regulation of immune cells, we performed an *in vitro* NK cell–cytotoxicity assay on the TRAMP-C2 WT versus *Pvrl2* KO cells. WT and *Pvrig* KO NK cells were mixed 1:1 with WT and *Pvrl2* KO TRAMP-C2 cells (**Fig. 5J**). PVRL2 loss in TRAMP-C2 cells significantly enhanced killing by both WT and *Pvrig* KO NK cells (**Fig. 5K**). In contrast, the loss of PVRIG had no significant impact on NK cell–mediated killing of WT TRAMP-C2 cells (**Fig. 5K**). Therefore, the PVRIG-independent roles of PVRL2 are through the direct regulation of immune cells, at least in the case of NK cells.

PVRL2 loss and TIGIT blockade function cooperatively to inhibit tumor growth

Some reports have suggested that PVRL2 can also bind and regulate TIGIT (17, 18). Therefore, we asked whether the PVRIG-independent function of PVRL2 could be through TIGIT. To do so, we injected WT MC38 cells into WT C57BL/6 mice followed by multiple injections of blocking anti-TIGIT (**Fig. 6A**). Anti-TIGIT led to a significant reduction in tumor growth and extension in survival (**Fig. 6B–D**). Next, we repeated the experiments in the *Pvrig* KO background to determine whether there was any collaborative effect of PVRIG with TIGIT underlying the immune suppressive role of PVRL2. With combined PVRIG loss and TIGIT blockade, *Pvrl2* KO still significantly retarded tumor growth and extended survival showing that PVRL2 can function independently of both PVRIG and TIGIT (**Fig. 6E–G**). Furthermore, combination of *Pvrig* KO plus anti-TIGIT blockade did not show any further inhibition of tumor growth or extension of survival relative to anti-TIGIT alone (Supplementary Fig. S4G). However, the combination of PVRL2 loss in the tumor cells with anti-TIGIT blockade showed a significantly greater effect than either alone (**Fig. 6E–G**). These data suggest that PVRL2 is not acting through TIGIT, but instead through a parallel pathway with both playing important roles in suppressing the antitumor immune response. In contrast, PVRIG appears to play a relatively minor role.

Given that antibody blockade can be incomplete, we further validated any potential role for TIGIT by using CRISPR mutagenesis to knock out the *Tigit* gene in *Pvrig* KO NK cells, and repeated *in vitro* NK cell–cytotoxicity assays on the TRAMP-C2 WT and *Pvrl2* KO cells (Supplementary Fig. S4H). Even in the absence of both PVRIG and TIGIT, PVRL2 loss showed an equally strong suppression of NK cell–mediated killing (Supplementary Fig. S4I and S4J). CD96 has also been suggested as a potential receptor for Nectin family proteins, although its immunoregulatory role has been controversial (21). Therefore, we also knocked out *Cd96* in *Pvrig* KO NK cells and performed the NK cell–cytotoxicity assay (Supplementary Fig. S4H). As with TIGIT, loss of CD96 together with PVRIG did not impact the ability of PVRL2 to suppress NK cell–mediated killing (Supplementary Fig. S4I and S4J). Together, these data show that PVRL2 is acting to suppress antitumor immunity through mechanisms that are independent of the Nectin family receptors PVRIG, TIGIT, and CD96 on immune cells.

Combined loss of PVRL2 and PVR does not further inhibit tumor growth

The PVRL2 paralog, PVR is believed to be the primary ligand of TIGIT (17, 18). Flow cytometry confirmed that the loss of PVRL2 in MC38 cells does not have an impact on PVR expression both *in vitro* and *in vivo* (Supplementary Fig. S5A–S5D). To test the impact of PVR loss alone and in combination with PVRL2 loss and/or TIGIT blockade, we used CRISPR/Cas9 mutagenesis to target the *Pvr* gene in MC38 cells. PVR loss was confirmed by flow cytometry (Supplementary Fig. S5A). The loss of PVR reduced tumor growth and extended survival, but to a lesser degree than loss of PVRL2 (**Fig. 7A–C**). This effect was through the immune system, as there was no difference in growth between WT and *Pvr* KO tumor cells in the immunodeficient NCG mouse background (Supplementary Fig. S5E and S5F). However, PVR appeared to have a similar effect on growth and survival in the *Rag1* KO versus WT mouse background, suggesting that PVR is functioning largely through the innate rather than adaptive immune response (**Fig. 7D–F**). Combining PVR loss with anti-TIGIT blockade showed no additional inhibition of tumor growth or extension of survival, demonstrating that all PVR activity in regulating tumor growth is through TIGIT and vice versa (**Fig. 7G–I**). Combination of PVR and PVRIG loss also showed no additional effect relative to PVR loss alone (Supplementary Fig. S5I–S5K). Next, we tested the combination of knocking out *Pvrl2* and *Pvr* in the same tumor cells, expecting it to phenocopy the combination of PVRL2 loss with anti-TIGIT blockade. However, there was no additive effect in tumor growth or survival (**Fig. 7A–C**). If anything, there was a slight increase in tumor growth in the double KO relative to *Pvrl2* KO alone, although this did not show in survival or in the *Rag1* KO background (**Fig. 7A–F**). All the cells produced tumors at a similar rate in NCG mice, confirming activity through targeting the antitumor immune response (Supplementary Fig. S5G and S5H). These data show that although PVR functions through TIGIT, combined loss of PVRL2 and PVR does not have the same positive impact as loss of PVRL2 combined with TIGIT blockade.

Discussion

Our results uncover a profound impact of PVRL2 on suppressing the antitumor immune response across multiple tumor models that is

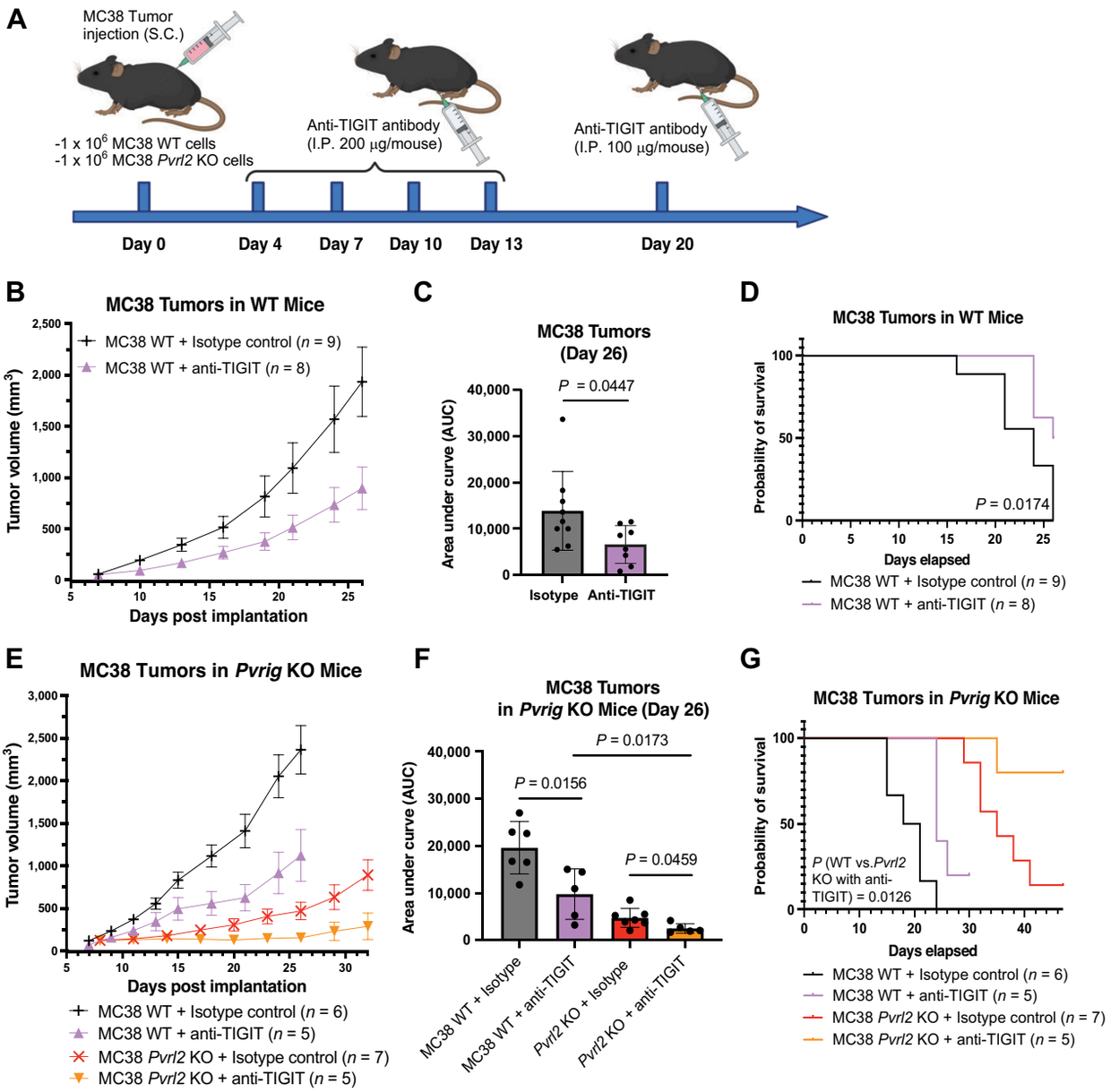

Figure 6.

PVRL2 loss and TIGIT blockade function cooperatively to inhibit tumor growth. **A,** Schematic of experiment design in **B**–**G**: After subcutaneous injection of 1×10^6 MC38 WT and *Pvrl2* KO cells in WT C57BL/6 or *Pvrig* KO mice, starting on day 4, mice were treated with serial doses of anti-TIGIT blocking antibody or isotype control at the indicated doses and schedule. **B,** Average tumor volume over time following subcutaneous injection of 1×10^6 MC38 WT cells with and without anti-TIGIT treatment in WT C57BL/6 mice. Error bars represent SEM. **C,** AUCs of the MC38 tumors from **B** on day 26. Dots represent individual mice. *P* value is calculated by unpaired *t* test. Error bars represent SD. **D,** Mouse survival curves following injections as described in **B**. *P* value is calculated by log-rank test. **E,** Average tumor volume over time following subcutaneous injection of 1×10^6 MC38 WT and *Pvrl2* KO cells with and without anti-TIGIT treatment in *Pvrig* KO mice. Error bars represent SEM. **F,** AUCs of the MC38 tumors from **E** on day 26. Dots represent individual mice. *P* values are calculated by unpaired *t* test. Error bars represent SD. **G,** Mouse survival curves following injections as described in **E**. *P* values are calculated by log-rank test.

largely independent of its known receptor, PVRIG. PVRL2 was initially identified in the late 1990s as an adhesion molecule belonging to the Nectin and Nectin-like family that supports cell-cell-junction formation (13, 52). In recent years, accumulating evidence has pointed toward a role for PVRL2 in cancer and the modulation of antitumor immunity (14, 18, 25, 44). Elevated levels of PVRL2 are found in many cancer types, including acute myeloid leukemia, multiple myeloma, and epithelial cancers such as colorectal cancer, melanoma, lung cancer, endometrial cancer, breast cancer, prostate cancer, and ovarian cancer (25, 53–56). While the function of PVRL2 in tumor development has been attributed to its ability to bind the coinhibitory receptor PVRIG on immune cells, there has been little evidence to support that

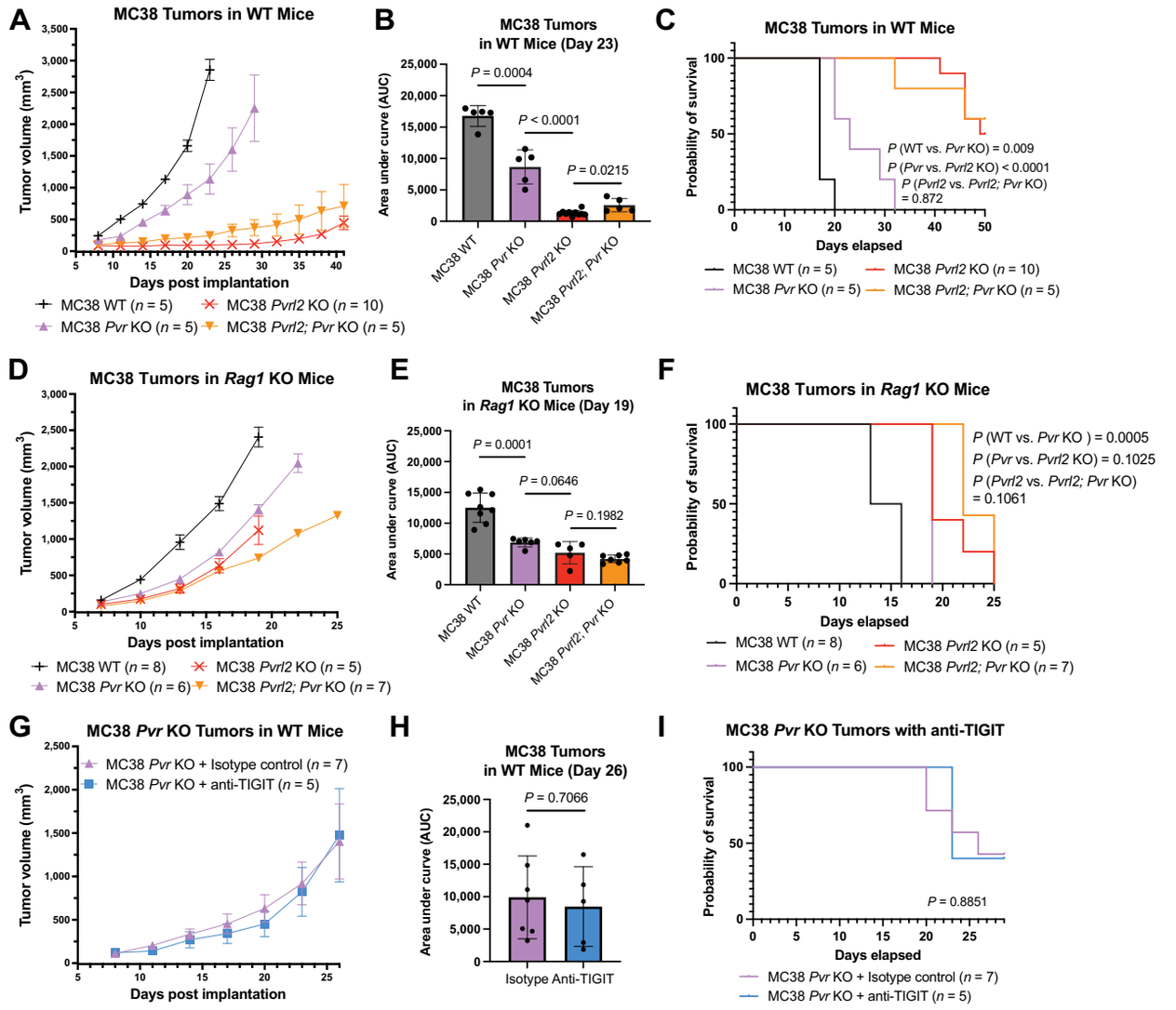

Figure 7.

Combined loss of PVRL2 and PVR loss does not further inhibit tumor growth. **A,** Average tumor volume over time following subcutaneous injection of 1×10^6 MC38 WT, *Pvrl2* KO, *Pvr* KO and *Pvrl2*; *Pvr* KO cells in WT C57BL/6 mice. Error bars represent SEM. **B,** AUCs of the MC38 tumors from **A** on day 23. Dots represent individual mice. *P* values are calculated by unpaired *t* test. Error bars represent SD. **C,** Mouse survival curves following injections as described in **A**. *P* values are calculated by log-rank test. **D,** Average tumor volume over time following subcutaneous injection of 1×10^6 MC38 WT, *Pvrl2* KO, *Pvr* KO and *Pvrl2*; *Pvr* KO cells in *Rag1* KO mice. Error bars represent SEM. **E,** AUCs of the MC38 tumors from **D** on day 19. Dots represent individual mice. *P* values are calculated by unpaired *t* test. Error bars represent SD. **F,** Mouse survival curves following injections as described in **D**. *P* values are calculated by log-rank test. **G,** Average tumor volume over time following subcutaneous injection of 1×10^6 MC38 *Pvr* KO cells with and without anti-TIGIT treatment in WT C57BL/6 mice. Error bars represent SEM. **H,** AUCs of the tumors from **G** on day 26. Dots represent individual mice. *P* value is calculated by unpaired *t* test. Error bars represent SD. **I,** Mouse survival curves following injections as described in **G**. *P* value is calculated by log-rank test.

conclusion *in vivo*. Previous research has been limited to *in vitro* experiments showing that anti-PVRL2 blockade can stimulate the activation of $CD8^+$ T cells when cocultured with the human melanoma Mel-624 cell line (25), or enhance PBMC-mediated lysis of hepatocellular carcinoma cell lines (57). To our knowledge, this study represents the first direct investigation into the mechanism of PVRL2 *in vivo* using *Pvrl2* KO mouse tumor models. Our data provide compelling evidence for the potential of PVRL2 as a therapeutic target.

Tumor-derived exosomes have emerged as an important mechanism by which tumor cells suppress antitumor immunity by carrying immunosuppressive molecules, such as PD-L1 (5, 6, 9, 10). Indeed, the expression of immunosuppressive molecules on exosomes has been identified as a potential biomarker for responses to ICIs in patients (58). In this study, we identify PVRL2 as another immune suppressive molecule on exosomes released by multiple human and mouse tumor cell lines, as well as primary prostate tumor tissue. Our *in vivo* experiments reveal that exosomal PVRL2 can significantly

promote tumor growth, although the contribution is relatively small compared with the substantial impact observed for PVRL2 on cells. This result indicates that the role of PVRL2 in promoting tumor growth primarily occurs though cell surface PVRL2 rather than via exosomes, which led us to focus on elucidating the mechanisms underlying the immunosuppressive role of cellular PVRL2 in tumor development.

By using multiple syngeneic mouse tumor models, we demonstrate that PVRL2 significantly promotes tumor growth and suppresses the antitumor immune response, with an even greater impact than that observed with PD-L1. Specifically, PVRL2 exerts its tumor-promoting effects by suppressing $CD8^+$ T cells and NK cells. However, our findings indicate the function of PVRL2 is predominantly independent of PVRIG, as evidenced by the minimal impact of PVRIG loss on the *Pvrl2* KO phenotype. Previous literatures have reported slower tumor growth in *Pvrig* KO mice for both MC38 and B16F10 tumors, although the difference was quite small (24, 50, 51). Our experiments similarly reveal slightly reduced growth of B16F10 WT tumors in *Pvrig* KO mice. However, we do not observe any impact on the growth of MC38 and TRAMP-C2 tumors with the loss of PVRIG. One potential explanation for this discrepancy is the difference in the number of tumor cells injected per mouse in our study (1 million cells) compared with the previous literatures (0.2 or 0.5 million cells). The higher tumor burden may overwhelm the suppressive properties of PVRIG, resulting in even less noticeable differences in tumor growth. Even in the absence of PVRIG, *Pvrl2* KO tumors grew much slower than their WT counterparts in all three models, even at the high tumor cell doses. Therefore, there must be additional receptor(s) for PVRL2. An obvious candidate is TIGIT given previous work suggesting low-affinity binding as well as upregulation of TIGIT on immune cells, particularly $CD8^+$ T cells, upon PVRIG blockade in coculture experiments with tumor cells (25). However, TIGIT blockade alone or in combination with PVRIG loss failed to inhibit the tumor-promoting impact of PVRL2. Thus, further studies will be required to uncover the primary receptor(s) that mediates PVRL2 function.

The primary ligand for TIGIT is the PVRL2 paralog PVR (17, 18). Indeed, we find that PVR function is lost with blockade of TIGIT and vice versa. Therefore, the ability of PVR to suppress the immune response appears to be entirely through TIGIT, in stark contrast to the PVRL2–PVRIG axis. The impact of PVRL2 loss on tumor growth was significantly greater than that of PVR loss. Furthermore, consistent with prior literature (59), we show that PVR appears to act predominantly through the innate immune response, as its impact on tumor growth was unaffected in the *Rag1* KO background, where there is no adaptive immune response. In contrast, we show that PVRL2 affects both the adaptive and innate immune responses presumably through direct regulation of $CD8^+$ T cells and NK cells, although discovery of the PVRL2 receptor(s) will be required to confirm that.

We found that the most profound suppressive effect on tumor growth was produced by a combination of PVRL2 loss and TIGIT blockade. However, this effect was not recapitulated with the combination of PVRL2 and PVR loss. If anything, the double KO led to slightly increased growth compared with PVRL2 loss alone. The most likely explanation for this seemingly contradictory finding is a role for the costimulatory receptor DNAM-1 in transmitting an immune-promoting signal from PVRL2 and PVR (14–16). It is possible the loss of either PVRL2 or PVR alone has little negative consequence on DNAM-1 activation, but the loss of both leads to loss of the immune-activating signal. In either case, the immune inhibitory functions of PVR and PVRL2 seem to be much greater than their immune promoting functions given that the double KO tumors still grow much slower than WT tumors.

Our preclinical results in mouse models provide strong evidence for the therapeutic potential of targeting PVRL2 to reactivate the antitumor immune response. Our data show that this potential therapeutic impact of PVRL2 inhibition can be further enhanced by TIGIT, but not PVR, blockade. Thus, our data provide strong rationale for combinatorial PVRL2 and TIGIT inhibition. In future studies, it will be important to determine how such dual inhibition will interact with anti-PD-1 or anti-PD-L1 blockade. Indeed, prior results have suggested cooperation between anti-TIGIT, anti-PVRIG, and anti-PD-1. Our data would suggest a substantially greater impact of anti-TIGIT, anti-PVRL2, and anti-PD-1.

Authors' Disclosures

J. Yang reports grants from NIH during the conduct of the study. L. Wang reports grants from NIH Common Fund during the conduct of the study. L.L. Kirkemo reports grants from NCI (1F31CA247527) outside the submitted work. C.D. Belair reports grants from NIH during the conduct of the study. L.L. Lanier advises Cullinan, Oncology, Dragonfly, DrenBio, Edity, GV20, IMIDomics, InnDura Therapeutics, Innovent, Nkarta, oNKo, Obsidian Therapeutics, and SBI Biotech to advance NK cell-based therapies. L. Fong reports grants and personal fees from Abbvie; grants from Bavarian Nordic, BMS, Janssen, Merck, and Roche Genentech; personal fees from Dendreon during the conduct of the study. R. Blelloch reports grants from NIH Common Fund during the conduct of the study. No disclosures were reported by the other authors.

Authors' Contributions

J. Yang: Conceptualization, data curation, formal analysis, validation, investigation, visualization, methodology, writing–original draft. **L. Wang:** Investigation. **J.R. Byrnes:** Investigation. **L.L. Kirkemo:** Investigation. **H. Driks:** Investigation. **C.D. Belair:** Investigation. **O.A. Aguilar:** Methodology. **L.L. Lanier:** Methodology. **J.A. Wells:** Supervision, funding acquisition. **L. Fong:** Supervision, funding acquisition. **R. Blelloch:** Conceptualization, resources, supervision, funding acquisition, project administration, writing–review and editing.

Acknowledgments

We thank all members of the UCSF Tumor Immunology Joint Meeting for helpful discussions and suggestions. We thank Carolyn Sangokoya, Ryan Boileau, Deniz Goekbuget for their helpful advice and feedback throughout the project. We thank Dr. Alexander Marson for kindly sharing the *Rag1* KO mice. We thank Dr. Jeffrey Schlom for kindly providing the MC38 cell line. We thank UCSF BIOS tissue bank for sharing the primary prostate tumor tissues. The project was funded by the NIH Common Fund Cancer Moonshot Program (Grant # U01CA244452).

Note

Supplementary data for this article are available at Cancer Immunology Research Online (http://cancerimmunolres.aacrjournals.org/).

Received August 31, 2023; revised January 4, 2024; accepted March 7, 2024; published first April 1, 2024.

References

1. Bagchi S, Yuan R, Engleman EG. Immune checkpoint inhibitors for the treatment of cancer: clinical impact and mechanisms of response and resistance. Annu Rev Pathol 2021;16:223–49.
2. Haslam A, Prasad V. Estimation of the percentage of US patients with cancer who are eligible for and respond to checkpoint inhibitor immunotherapy drugs. JAMA Netw Open 2019;2:e192535.

3. Das S, Johnson DB. Immune-related adverse events and anti-tumor efficacy of immune checkpoint inhibitors. J Immunother Cancer 2019;7:306.
4. Sharma P, Hu-Lieskovan S, Wargo JA, Ribas A. Primary, adaptive, and acquired resistance to cancer immunotherapy. Cell 2017;168:707–23.
5. Poggio M, Hu T, Pai C-C, Chu B, Belair CD, Chang A, et al. Suppression of exosomal PD-L1 induces systemic anti-tumor immunity and memory. Cell 2019; 177:414–27.
6. Chen G, Huang AC, Zhang W, Zhang G, Wu M, Xu W, et al. Exosomal PD-L1 contributes to immunosuppression and is associated with anti-PD-1 response. Nature 2018;560:382–6.
7. Kalluri R, McAndrews KM. The role of extracellular vesicles in cancer. Cell 2023; 186:1610–26.
8. van Niel G, D'Angelo G, Raposo G. Shedding light on the cell biology of extracellular vesicles. Nat Rev Mol Cell Biol 2018;19:213–28.
9. Chen J, Song Y, Miao F, Chen G, Zhu Y, Wu N, et al. PDL1-positive exosomes suppress antitumor immunity by inducing tumor-specific CD8(+) T cell exhaustion during metastasis. Cancer Sci 2021;112:3437–54.
10. Yang Y, Li C-W, Chan L-C, Wei Y, Hsu J-M, Xia W, et al. Exosomal PD-L1 harbors active defense function to suppress T cell killing of breast cancer cells and promote tumor growth. Cell Res 2018;28:862–4.
11. Johnston RJ, Lee PS, Strop P, Smyth MJ. Cancer immunotherapy and the nectin family. Ann Rev Cancer Biol 2021;5:203–19.
12. Alteber Z, Kotturi MF, Whelan S, Ganguly S, Weyl E, Pardoll DM, et al. Therapeutic targeting of checkpoint receptors within the DNAM1 axis. Cancer Discov 2021;11:1040–51.
13. Lopez M, Aoubala M, Jordier F, Isnardon D, Gomez S, Dubreuil P, et al. The human poliovirus receptor related 2 protein is a new hematopoietic/endothelial homophilic adhesion molecule. Blood 1998;92:4602–11.
14. Bottino C, Castriconi R, Pende D, Rivera P, Nanni M, Carnemolla B, et al. Identification of PVR (CD155) and Nectin-2 (CD112) as cell surface ligands for the human DNAM-1 (CD226) activating molecule. J Exp Med 2003;198: 557–67.
15. Tahara-Hanaoka S, Shibuya K, Onoda Y, Zhang H, Yamazaki S, Miyamoto A, et al. Functional characterization of DNAM-1 (CD226) interaction with its ligands PVR (CD155) and nectin-2 (PRR-2/CD112). Int Immunol 2004; 16:533–8.
16. Shibuya A, Campbell D, Hannum C, Yssel H, Franz-Bacon K, McClanahan T, et al. DNAM-1, a novel adhesion molecule involved in the cytolytic function of T lymphocytes. Immunity 1996;4:573–81.
17. Yu X, Harden K, Gonzalez LC, Francesco M, Chiang E, Irving B, et al. The surface protein TIGIT suppresses T cell activation by promoting the generation of mature immunoregulatory dendritic cells. Nat Immunol 2009;10:48–57.
18. Stanietsky N, Simic H, Arapovic J, Toporik A, Levy O, Novik A, et al. The interaction of TIGIT with PVR and PVRL2 inhibits human NK cell cytotoxicity. Proc Natl Acad Sci U S A 2009;106:17858–63.
19. Zhu Y, Paniccia A, Schulick AC, Chen W, Koenig MR, Byers JT, et al. Identification of CD112R as a novel checkpoint for human T cells. J Exp Med 2016; 213:167–76.
20. Blake SJ, Stannard K, Liu J, Allen S, Yong MCR, Mittal D, et al. Suppression of metastases using a new lymphocyte checkpoint target for cancer immunotherapy. Cancer Discov 2016;6:446–59.
21. Chan CJ, Martinet L, Gilfillan S, Souza-Fonseca-Guimaraes F, Chow MT, Town L, et al. The receptors CD96 and CD226 oppose each other in the regulation of natural killer cell functions. Nat Immunol 2014;15:431–8.
22. Fuchs A, Cella M, Giurisato E, Shaw AS, Colonna M. Cutting edge: CD96 (tactile) promotes NK cell-target cell adhesion by interacting with the poliovirus receptor (CD155). J Immunol 2004;172:3994–8.
23. Seth S, Maier MK, Qiu Q, Ravens I, Kremmer E, Förster R, et al. The murine pan T cell marker CD96 is an adhesion receptor for CD155 and nectin-1. Biochem Biophys Res Commun 2007;364:959–65.
24. Murter B, Pan X, Ophir E, Alteber Z, Azulay M, Sen R, et al. Mouse PVRIG Has CD8(+) T cell-specific coinhibitory functions and dampens antitumor immunity. Cancer Immunol Res 2019;7:244–56.
25. Whelan S, Ophir E, Kotturi MF, Levy O, Ganguly S, Leung L, et al. PVRIG and PVRL2 are induced in cancer and inhibit CD8(+) T-cell function. Cancer Immunol Res 2019;7:257–68.
26. Lozano E, Dominguez-Villar M, Kuchroo V, Hafler DA. The TIGIT/CD226 axis regulates human T cell function. J Immunol 2012;188:3869–75.
27. Johnston RJ, Comps-Agrar L, Hackney J, Yu X, Huseni M, Yang Y, et al. The immunoreceptor TIGIT regulates antitumor and antiviral CD8(+) T cell effector function. Cancer Cell 2014;26:923–37.
28. Rousseau A, Parisi C, Barlesi F. Anti-TIGIT therapies for solid tumors: a systematic review. ESMO Open 2023;8:101184.
29. Dumbrava E, Sharma M, Fleming G, Papadopoulos K, Sullivan R, Vaena D, et al. 478 COM701 in combination with BMS-986207 (anti-TIGIT antibody) and nivolumab – preliminary results of safety, tolerability and pharmacokinetics in patients with advanced solid tumors (NCT04570839). J Immunother Cancer 2021;9:A508.
30. Vaena DA, Fleming GF, Chmielowski B, Sharma M, Hamilton EP, Sullivan RJ, et al. COM701 with or without nivolumab: results of an ongoing phase 1 study of safety, tolerability and preliminary antitumor activity in patients with advanced solid malignancies (NCT03667716). J Clin Oncol 39: 15s, 2021 (suppl; abstr 2504).
31. Kaighn ME, Narayan KS, Ohnuki Y, Lechner JF, Jones LW. Establishment and characterization of a human prostatic carcinoma cell line (PC-3). Invest Urol 1979;17:16–23.
32. Carey TE, Takahashi T, Resnick LA, Oettgen HF, Old LJ. Cell surface antigens of human malignant melanoma: mixed hemadsorption assays for humoral immunity to cultured autologous melanoma cells. Proc Natl Acad Sci U S A 1976;73: 3278–82.
33. Foster BA, Gingrich JR, Kwon ED, Madias C, Greenberg NM. Characterization of prostatic epithelial cell lines derived from transgenic adenocarcinoma of the mouse prostate (TRAMP) model. Cancer Res 1997;57:3325–30.
34. Griswold DP, Corbett TH. A colon tumor model for anticancer agent evaluation. Cancer 1975;36:2441–4.
35. Fidler IJ. The relationship of embolic homogeneity, number, size and viability to the incidence of experimental metastasis. Eur J Cancer (1965) 1973;9:223–7.
36. Corbett TH, Griswold DP Jr, Roberts BJ, Peckham JC, Schabel FM Jr. Tumor induction relationships in development of transplantable cancers of the colon in mice for chemotherapy assays, with a note on carcinogen structure. Cancer Res 1975;35:2434–9.
37. Maund SL, Nolley R, Peehl DM. Optimization and comprehensive characterization of a faithful tissue culture model of the benign and malignant human prostate. Lab Invest 2014;94:208–21.
38. Solomon PE, Kirkemo LL, Wilson GM, Leung KK, Almond MH, Sayles LC, et al. Discovery proteomics analysis determines that driver oncogenes suppress antiviral defense pathways through reduction in interferon-β autocrine stimulation. Mol Cell Proteomics 2022;21:100247.
39. Byrnes JR, Weeks AM, Shifrut E, Carnevale J, Kirkemo L, Ashworth A, et al. Hypoxia is a dominant remodeler of the effector T cell surface proteome relative to activation and regulatory T cell suppression. Mol Cell Proteomics 2022;21: 100217.
40. Kirkemo LL, Elledge SK, Yang J, Byrnes JR, Glasgow JE, Blelloch R, et al. Cell-surface tethered promiscuous biotinylators enable comparative small-scale surface proteomic analysis of human extracellular vesicles and cells. eLife 2022;11:e73982.
41. Szklarczyk D, Gable AL, Nastou KC, Lyon D, Kirsch R, Pyysalo S, et al. The STRING database in 2021: customizable protein-protein networks, and functional characterization of user-uploaded gene/measurement sets. Nucleic Acids Res 2021;49:D605–D12.
42. Aguilar OA, Fong LK, Ishiyama K, DeGrado WF, Lanier LL. The CD3ζ adaptor structure determines functional differences between human and mouse CD16 Fc receptor signaling. J Exp Med 2022;219:e20220022.
43. Perez-Riverol Y, Bai J, Bandla C, García-Seisdedos D, Hewapathirana S, Kamatchinathan S, et al. The PRIDE database resources in 2022: a hub for mass spectrometry-based proteomics evidences. Nucleic Acids Res 2022;50: D543–D52.
44. Stamm H, Klingler F, Grossjohann E-M, Muschhammer J, Vettorazzi E, Heuser M, et al. Immune checkpoints PVR and PVRL2 are prognostic markers in AML and their blockade represents a new therapeutic option. Oncogene 2018;37: 5269–80.
45. Sugamura K, Asao H, Kondo M, Tanaka N, Ishii N, Ohbo K, et al. The interleukin-2 receptor gamma chain: its role in the multiple cytokine receptor complexes and T cell development in XSCID. Annu Rev Immunol 1996;14:179–205.
46. Schuler W, Weiler IJ, Schuler A, Phillips RA, Rosenberg N, Mak TW, et al. Rearrangement of antigen receptor genes is defective in mice with severe combined immune deficiency. Cell 1986;46:963–72.
47. Yamauchi T, Takenaka K, Urata S, Shima T, Kikushige Y, Tokuyama T, et al. Polymorphic sirpa is the genetic determinant for NOD-based mouse lines to achieve efficient human cell engraftment. Blood 2013; 121:1316–25.
48. Heng TSP, Painter MW; The Immunological Genome Project Consortium. The immunological genome project: networks of gene expression in immune cells. Nat Immunol 2008;9:1091–4.

49. Xu F, Sunderland A, Zhou Y, Schulick RD, Edil BH, Zhu Y. Blockade of CD112R and TIGIT signaling sensitizes human natural killer cell functions. Cancer Immunol Immunother 2017;66:1367–75.
50. Li J, Whelan S, Kotturi MF, Meyran D, D'Souza C, Hansen K, et al. PVRIG is a novel natural killer cell immune checkpoint receptor in acute myeloid leukemia. Haematologica 2020;106:3115–24.
51. Li Y, Zhang Y, Cao G, Zheng X, Sun C, Wei H, et al. Blockade of checkpoint receptor PVRIG unleashes anti-tumor immunity of NK cells in murine and human solid tumors. J Hematol Oncol 2021;14:100.
52. Harrison OJ, Vendome J, Brasch J, Jin X, Hong S, Katsamba PS, et al. Nectin ectodomain structures reveal a canonical adhesive interface. Nat Struct Mol Biol 2012;19:906–15.
53. Casado JG, Pawelec G, Morgado S, Sanchez-Correa B, Delgado E, Gayoso I, et al. Expression of adhesion molecules and ligands for activating and costimulatory receptors involved in cell-mediated cytotoxicity in a large panel of human melanoma cell lines. Cancer Immunol Immunother 2009;58:1517–26.
54. Mastaglio S, Wong E, Perera T, Ripley J, Blombery P, Smyth MJ, et al. Natural killer receptor ligand expression on acute myeloid leukemia impacts survival and relapse after chemotherapy. Blood Adv 2018;2:335–46.
55. Sanchez-Correa B, Gayoso I, Bergua JM, Casado JG, Morgado S, Solana R, et al. Decreased expression of DNAM-1 on NK cells from acute myeloid leukemia patients. Immunol Cell Biol 2012;90:109–15.
56. El-Sherbiny YM, Meade JL, Holmes TD, McGonagle D, Mackie SL, Morgan AW, et al. The requirement for DNAM-1, NKG2D, and NKp46 in the natural killer cell-mediated killing of myeloma cells. Cancer Res 2007;67:8444–9.
57. Li A, Ji B, Yang Y, Ye B, Zhu Q, Hu X, et al. Single-cell RNA sequencing highlights the role of PVR/PVRL2 in the immunosuppressive tumour microenvironment in hepatocellular carcinoma. Front Immunol 2023;14:1164448.
58. Akbar S, Raza A, Mohsin R, Kanbour A, Qadri S, Parray A, et al. Circulating exosomal immuno-oncological checkpoints and cytokines are potential biomarkers to monitor tumor response to anti-PD-1/PD-L1 therapy in non-small cell lung cancer patients. Front Immunol 2022;13:1097117.
59. Zhang Q, Bi J, Zheng X, Chen Y, Wang H, Wu W, et al. Blockade of the checkpoint receptor TIGIT prevents NK cell exhaustion and elicits potent anti-tumor immunity. Nat Immunol 2018;19:723–32.